Calibration and simulations of SIXS-P's response to energetic particles

Master's Thesis
University of Turku
Department of Physics
and Astronomy
Physics
2016
Erkka Heino
Referees:
Prof. Rami Vainio
M.Sc. Esa Riihonen

UNIVERSITY OF TURKU
Department of Physics and Astronomy

HEINO, ERKKA Calibration and simulations of SIXS-P's response to energetic particles

Master's Thesis, 70 p.
Physics
August 2016

The Solar Intensity X-ray and particle Spectrometer (SIXS) on board BepiColombo's Mercury Planetary Orbiter (MPO) will study solar energetic particles moving towards Mercury and solar X-rays on the dayside of Mercury. The SIXS instrument consists of two detector sub-systems; X-ray detector SIXS-X and particle detector SIXS-P. The SIXS-P subdetector will detect solar energetic electrons and protons in a broad energy range using a particle telescope approach with five outer Si detectors around a central CsI(Tl) scintillator. The measurements made by the SIXS instrument are necessary for other instruments on board the spacecraft. SIXS data will be used to study the Solar X-ray corona, solar flares, solar energetic particles, the Hermean magnetosphere, and solar eruptions.

The SIXS-P detector was calibrated by comparing experimental measurement data from the instrument with Geant4 simulation data. Calibration curves were produced for the different side detectors and the core scintillator for electrons and protons, respectively. The side detector energy response was found to be linear for both electrons and protons. The core scintillator energy response to protons was found to be non-linear. The core scintillator calibration for electrons was omitted due to insufficient experimental data.

The electron and proton acceptance of the SIXS-P detector was determined with Geant4 simulations. Electron and proton energy channels are clean in the main energy range of the instrument. At higher energies, protons and electrons produce non-ideal response in the energy channels.

Due to the limited bandwidth of the spacecraft's telemetry, the particle measurements made by SIXS-P have to be pre-processed in the data processing unit of the SIXS instrument. A lookup table was created for the pre-processing of data with Geant4 simulations, and the ability of the lookup table to provide spectral information from a simulated electron event was analysed. The lookup table produces clean electron and proton channels and is able to separate protons and electrons. Based on a simulated solar energetic electron event, the incident electron spectrum cannot be determined from channel particle counts with a standard analysis method.

Keywords: BepiColombo, Particle detection, Instrumentation, Geant4, Simulation

Contents

Introduction

BepiColombo is a two-spacecraft interdisciplinary mission to Mercury, conducted jointly by the European Space Agency (ESA) and the Japanese Aerospace Exploration Agency (JAXA). Instruments on board BepiColombo will make comprehensive and accurate observations of Mercury's magnetospheric and exospheric dynamics and their interactions with solar radiation and interplanetary dust. The mission will complement observations made by National Aeronautics and Space Administration's (NASA) MErcury Surface, Space ENvironment, GEochemistry and Ranging (MESSENGER) mission (2004–2015).

The Solar Intensity X-ray and particle Spectrometer (SIXS) on board BepiColombo's Mercury Planetary Orbiter (MPO) will investigate solar energetic protons and electrons moving towards Mercury and solar X-rays on the dayside of Mercury. The data from the measurements will be used to investigate Mercury's X-ray emissions, solar X-ray corona, solar flares, solar energetic particles (SEPs), the Hermean magnetosphere and solar eruptions. Observations made by SIXS are crucial for other instruments on board BepiColombo.

SIXS comprises two detector sub-systems; X-ray detector SIXS-X and particle detector SIXS-P. SIXS-X has three identical Si PIN detectors for measuring solar X-rays in a nominal energy range 1 keV–20 keV. The particle detector assembly consists of five thin Si detectors around a central CsI(Tl) scintillator. The nominal energy ranges of detected electrons and protons are 100 keV–3 MeV and 1 MeV–30 MeV, respectively. The mechanical structure and scientific goals of the SIXS detector are presented in section 2.3.

The SIXS-P subdetector measures the energy loss of the incident particles in the outer Si detectors and in the core scintillator. The measured energy losses are analysed using the $\Delta E - E$ method to identify the detected particles and determine their energies. The theory behind measuring energy loss of particles and the $\Delta E - E$ method are presented in sections 2.1 and 2.2. The structure, scientific goals, particle detection method, and the onboard data handling of SIXS-P are presented in section 2.3.

In order to provide reliable measurements and data, which can be compared

and used by other instruments, the instruments have to be calibrated. The energy response calibration of the SIXS-P instrument is presented in this thesis. The calibration was done by comparing experimental data measured by Aboa Space Research Oy (ASRO) with Geant4 simulation data. Experimental proton data were measured at particle accelerator facilities in Jyväskylä (15 MeV $\leq E \leq$ 40 MeV) and Kumpula ($E \leq$ 10 MeV). Experimental electron data were measured at an electron gun facility in Kiel ($E \leq$ 100 keV), and as laboratory measurements using radioactive sources and a magnetic deflector. The calibration method is explained in section 2.4 and the calibration of the instrument is presented in section 3.3.

The particle response of the SIXS-P detector was studied to determine how the different electron and proton channels respond to particles of different energies. The acceptance of the detector was simulated with a flat energy spectrum for electrons and protons. The acceptance simulations are presented in section 3.4. The simulated response of the detector to cosmic ray proton and quiet time electron spectra is presented in section 3.5.

Due to the limited bandwidth of BepiColombo's telemetry, the measured raw data of the SIXS-P instrument has to be pre-processed in the SIXS instrument. The measured particle events are designated into predefined energy channels using a lookup table. The energy channel counts are used to create particle spectra and anisotropy distributions that are sent back to the Earth. The methods used to create the lookup table and its particle response are presented in chapter 4. An intense electron event, measured by the EPS instrument of the MESSENGER spacecraft, was analysed with the lookup table to determine how well the incoming electron spectrum can be inferred from the electron energy channel counts. The analysis of this event is presented in section 4.3.

1 Background

1.1 History

Mercury is the closest planet to the Sun with a perihelion of only 0.307 AU. Due to its proximity to the Sun, observation of Mercury from Earth is difficult. The proximity of Mercury to the Sun also poses difficulties for spacecraft missions as Mercury is deep in the Sun's gravitational well and the spacecraft has to use large amounts of energy to decelerate to an orbit closer to the Sun. More energy is needed to reach Mercury than for a mission to Pluto [1]. The thermal environment at Mercury is harsh, because of the increased solar irradiance and thermal radiation from the dayside of the planet [2].

Despite advancements in technology and space flight, there have been few missions to Mercury. Prior to 2008, the only spaceborne observations of Mercury were made by NASA's Mariner 10 spacecraft. Launched between 1962 and 1973, the ten Mariner space probes were NASA's primary planetary exploration missions.

The initial mission of Mariner 10 was to fly to Venus and Mercury using gravity-assist flybys. Originally only one Mercury flyby was planned, but Italian Giuseppe 'Bepi' Colombo (1920–1984) recognised the possibility of a transfer to a resonant multiple flyby orbit [2]. Due to Colombo's sizeable contributions to planetary research, space flight and celestial mechanics, the BepiColombo mission was named in his honour [1]. Mariner 10 performed a total of three Mercury flybys in 1974–1975, discovering the planet's magnetosphere and providing pictures of the planet surface [3]. The Mariner 10 flybys provided the largest amount of information on Mercury, prior to NASA's MESSENGER mission.

The MErcury Surface, Space ENvironment, GEochemistry and Ranging (MESSENGER) spacecraft was launched in August 2004. MESSENGER performed three flybys of Mercury before entering Hermean orbit in March 2011. MESSENGER spent 4.1 years in orbit around Mercury and intentionally impacted Mercury's surface in April 2015 [4]. During its mission, the MESSENGER spacecraft provided an

unprecedented amount of accurate long-time data from Mercury [5].

1.2 BepiColombo

In the year 2000, BepiColombo was accepted by ESA's Science Programme Committee as a Cornerstone class mission of its Horizons 2000 scientific programme plan. The mission was to launch between 2007 and 2009. Japan's Institute for Space and Astronautical Sciences (ISAS, later a part of JAXA) examined the possibility of a Mercury orbiter and joined the BepiColombo mission [6].

The original system architecture featured three separate spacecraft elements: the Mercury Planetary Orbiter (MPO), the Mercury Magnetospheric Orbiter (MMO) and the Mercury Surface Element (MSE) lander [6]. Two different launch possibilities were considered; a single launch with an Ariane 5 rocket or two separate launches with the Soyuz-Fregat rocket [7]. In further studies the mass and monetary costs of MSE were deemed too high and the lander element was removed from the mission design.

In 2004, after a reassessment of the mission in 2002–2003, ESA approved a mission design featuring two orbiters with a single launch. The payloads for the Japanese MMO and the European MPO were approved in 2004 [2]. BepiColombo will be launched in August 2018 and will arrive at Mercury in late 2024 [8].

1.2.1 System configuration and mission overview

The space segment of BepiColombo comprises the following segments [1]:

Mercury Transfer Module (MTM) Module for propulsion during the cruise phase.

Mercury Planetary Orbiter (MPO) Houses remote sensing and in-situ particle, magnetometry and radio science instruments.

Mercury Magnetospheric Orbiter (MMO) Houses instruments for measuring electromagnetic fields and waves, and charged, neutral and dust particles in-situ, as well as one remote sensing instrument.

MMO Sunshield and Interface Structure (MOSIF) Provides thermal protection for the MMO during the cruise phase.

BepiColombo will utilise a solar electric propulsion system that, in conjunction with low-thrust arcs and flybys at Earth, Venus and Mercury, will enable a low relative velocity approach to Mercury. This method will provide flexibility to the design of the trajectory at a very low propellant cost [1].

The composite spacecraft (the whole space segment) will be launched on a direct escape trajectory towards Mercury. The spacecraft will conduct two Venus flybys and four Mercury flybys. The flybys and a series of low-thrust arcs will reduce the relative velocity and the spacecraft will be weakly captured by Mercury before an insertion manoeuvre. The insertion manoeuvre will be done with MPO's chemical thrust system. After the insertion manoeuvre, the spacecraft will reach MMO's intended orbit, where the MMO will be jettisoned. The remaining spacecraft will then conduct an additional thrust phase with the chemical propulsion system to reach MPO's intended orbit [8]. MMO and MPO will be on polar orbits to achieve full coverage of Mercury [1]. The mission time in Mercury is one year with an optional one year extension [8].

1.2.2 Scientific goals

BepiColombo will concentrate on conducting accurate and thorough long-term measurements to complement previous measurements, rather than look for evidence of new physical phenomena. The main scientific goals to be studied during the BepiColombo mission as listed in [1] and [6] are:

- the origin and evolution of a planet close to its partner star;
- Mercury's form, interior structure, composition;
- the exogenic and endogenic surface modifications, cratering, tectonics and volcanism;
- the composition, origin and dynamics of Mercury's exosphere and polar deposits;
- the structure and dynamics of the Hermean magnetosphere;
- test of Einstein's theory of general relativity.

The scientific goals can be divided into five major topical areas: interior, surface, exosphere, magnetosphere and fundamental physics. The SIXS instrument will provide data for the instruments relating to the surface, exosphere and magnetosphere of Mercury. In addition to providing data for other instruments, measurements made by SIXS can be used to study particle acceleration and transport, space weather, solar eruptions, solar flares, and the solar X-ray corona [1, 9, 10].

The measurements of solar X-rays and solar energetic particles moving towards Mercury are crucial for the Mercury Imaging X-ray Spectrometer (MIXS). MIXS will measure fluorescent X-ray emissions from the surface of Mercury to study the elemental composition of Mercury's surface. The X-ray fluorescence is produced by excitations caused by solar X-rays and solar energetic particles hitting the surface of the planet [11]. In essence, SIXS will measure the fluxes and energies of solar X-rays and energetic particles hitting Mercury's surface and MIXS will measure the fluorescent X-ray emission caused by the incident solar X-rays and particles. The element composition of Mercury's surface can be used to study the evolution of the planet.

The particle flux data from SIXS can also be used in conjunction with particle data from instruments in the MMO to study Mercury's magnetospheric activity [9].

2 Theory

This chapter covers topics necessary to understand the research presented in this thesis. The general theory of particle interactions in matter is presented in the first section. The following sections cover the mechanical structure, scientific goals, and onboard data handling of SIXS-P. The last section of this chapter presents a method for calibrating the energy response of the instrument.

2.1 Passage of charged particles in matter

Charged particles lose energy as they pass through matter, and this energy loss is the basis for detecting particles. Electrons and heavy particles ($m \geq m_p$) act differently when passing through matter due to their large mass difference. Due to their larger mass, heavy particles are accelerated less than electrons by the Coulomb force.

The main energy loss mechanism for protons in the simulated main energy range (< 100 MeV) is the ionisation and excitation of atoms. In this case, protons lose their energy in inelastic collisions with electrons of the medium. The average energy loss in these interactions is described by the Bethe formula. At higher energies, heavy particles can lose their energy in inelastic collisions with the medium's nuclei (hadronic interactions). This method of energy loss becomes significant at energies of a few hundred megaelectron-volts. The passage of heavy particles in matter is described in the first part of this section.

Electrons lose their energy through collisions and radiative processes. The main collisional energy loss mechanism for electrons is ionisation of the atoms and molecules of the medium. The main radiative energy loss process for electrons is Bremsstrahlung. The dominant energy loss mechanism for electrons in the SIXS-P detector's materials, and the simulated main energy range (< 6 MeV), is ionisation. Passage of electrons in matter is described in the second part of this section.

The differences in the passage of electrons and heavier charged particles in matter can be used to identify the particle. One way to use particle interactions to identify

and measure particle energies is the $\Delta E - E$ method, which is described shortly in the third part of this section.

The presented description of the passage of charged particles in matter is based on [12].

2.1.1 Heavy particles

As heavy particles pass through matter they lose energy through Coulomb interactions with the electrons and nuclei of the atoms of the medium. In collisions with nuclei, heavy particles lose a small amount of energy, but their direction can change considerably. In collisions with the electrons of the medium, heavy particles transfer a large net amount of energy to the electrons, but the direction of the particles changes only by a small amount. Due to this difference, the main cause for the energy loss of heavy particles in matter are the collisions with electrons. The main reason for changes in direction of heavy particles are due to collisions with nuclei.

The rate of energy loss of particles in matter depends on the properties of the matter and the properties of the particle. The energy loss rate in a certain material is called stopping power. Stopping power S is defined as the energy loss of a particle dE in one unit length dx of material. The total stopping power of a material is the sum of stopping powers due to interactions with electrons and nuclei:

$$S_{\text{tot}} = -\frac{dE}{dx} = S_{\text{electrons}} + S_{\text{nuclei}}. \tag{2.1.1.1}$$

The nuclei component of the stopping power can be neglected at low energies.

Niels Bohr (1885–1962) derived the first relation for the energy loss of ions moving in the electromagnetic field of electrons. Bohr considered the impulses of the ion to the electrons as it passes through matter. Hans Bethe (1906–2005) derived a relation for the energy loss using a quantum mechanical approach:

$$\left[-\frac{dE}{dx}\right] = 4\pi N_A r_e^2 m_e c^2 \rho \frac{Z}{A}\frac{z^2}{\beta^2}\left[\ln\left(\frac{W_{\max}}{I}\right) - \beta^2\right], \tag{2.1.1.2}$$

where:

N_A	Avogadro's number
r_e	classical radius of an electron
m_e	rest mass of an electron
ρ	density of the medium
Z	charge number of the medium
A	mass number of the medium
z	charge number of the ion
β	velocity of the ion in units of c
$W_{\max}$	maximum energy transfer in a single collision
I	mean excitation potential or ionisation potential of the medium

The maximum energy transfer in a single collision $W_{\max}$ can be expressed as

$$W_{\max} \approx 2m_e c^2 \gamma^2 \beta^2 = 2m_e c^2 \frac{\beta^2}{1-\beta^2}, \tag{2.1.1.3}$$

when the mass of the particle is much larger than the mass of the electron and γ is the Lorentz factor. The mean excitation potential of a medium is given by the experimental formulas

$$I = 12Z + 7.2 \text{ eV, when } Z < 13 \tag{2.1.1.4}$$

$$I = 9.76Z + 5.58Z^{-1.19} \text{ eV, when } Z \geq 13. \tag{2.1.1.5}$$

The Bethe formula (2.1.1.2) breaks down at very high and moderately low energies. Two correction terms have to be implemented because of this. The density effect correction δ takes into account the shielding caused by distant electrons because of the polarisation of electrons of the medium by the electric field of the moving ion. Collisions with the distant electrons contribute less to the total energy loss than predicted by equation (2.1.1.2). The shielding depends on the electron density of the medium and the density effect correction becomes more important as the energy of the ions increases. The shell correction term C corrects for ions with velocities comparable, or smaller than the orbital velocity of the bound electrons. At these velocities, the initial assumption in (2.1.1.2) that the bound electrons are stationary in relation to the incident particle, is no longer valid. Using these correction terms

the Bethe formula can be expressed as:

$$\left[-\frac{dE}{dx}\right] = 4\pi N_A r_e^2 m_e c^2 \rho \frac{Z}{A}\frac{z^2}{\beta^2}\left[\ln\left(\frac{W_{\max}}{I}\right) - \beta^2 - \frac{\delta}{2} - \frac{C}{Z}\right], \tag{2.1.1.6}$$

The Bethe formula is only valid for pure elements. For compounds or mixtures of multiple different elements, the Bragg-Kleeman rule can be utilized. The total stopping power in a compound material is:

$$-\frac{dE}{dx} = \sum_{i=1}^{n}\left(w_i\left[\frac{dE}{dx}\right]_i\right), \tag{2.1.1.7}$$

where w_i is the fraction of element i by mass in the compound material.

2.1.2 Electrons

As electrons pass through matter, they lose energy rapidly in collisional interactions and decelerate. The deceleration of the electrons causes a radiative process called Bremsstrahlung. The ionisation and excitation of atoms is the main energy loss mechanism for electrons at low to moderate energies. The direction of electrons passing through matter changes constantly due to collisional interactions. This constant change of direction causes electrons to backscatter and to have complex tracks in the material they pass through. Above a critical particle energy Bremsstrahlung becomes the dominant energy loss mechanism. The fractional energy loss of electrons and positrons as a function of particle energy in lead, due to different energy loss mechanisms is shown in Figure 2.1.

The stopping power of a material for electrons consists of two terms; collisional and radiative:

$$S_{\text{electrons}} = S_{\text{collisional}} + S_{\text{radiative}}. \tag{2.1.2.1}$$

The collisional component consists of all the collisional processes, not only the inelastic impact ionisation process.

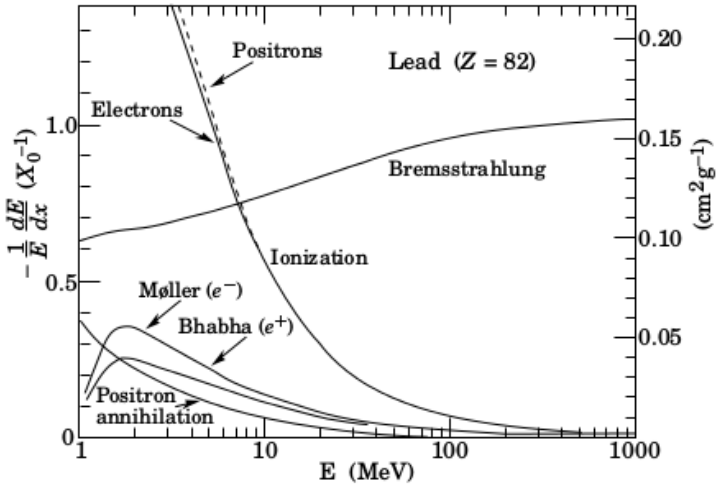

Figure 2.1: Fractional energy loss of electrons and positrons per radiation length in lead as a function of particle energy [12, p. 122]. The radiative energy loss becomes the dominant form of energy loss in lead at approximately 7 MeV.

The collisional component can be written as

$$\left[-\frac{dE}{dx}\right]_{\text{collisional}} = \frac{2\pi Z e^4 \rho}{m_e v^2}\left[\ln\left(\frac{m_e v^2 E}{2I^2(1-\beta^2)}\right) - \ln 2\left(2\sqrt{1-\beta^2} - 1 + \beta^2\right) + (1-\beta^2) + \frac{1}{8}\left(1-\sqrt{1-\beta^2}\right)^2\right]. \tag{2.1.2.2}$$

The radiative component is:

$$\left[-\frac{dE}{dx}\right]_{\text{radiative}} = \frac{Z(Z+1)e^4 \rho E}{137 m_e^2 c^4}\left[4\ln\left(\frac{2E}{m_e c^2} - \frac{4}{3}\right)\right] \tag{2.1.2.3}$$

Thus the collisional and radiative processes behave at relativistic energies as

$$S_{\text{collisional}} \propto \ln(E) \tag{2.1.2.4}$$

$$S_{\text{radiative}} \propto E. \tag{2.1.2.5}$$

The radiative energy losses increase more rapidly than the collisional energy losses as the incident energy increases. At a critical energy, the collisional and radiative energy losses are equal. Below the critical energy, the main energy loss mechanism is the collisional Coulomb scattering. Above the critical energy, the radiative energy loss is the dominant form of energy loss. The critical energy can be approximated

by the ratio of the total stopping power components (2.1.2.2) and (2.1.2.3):

$$\frac{S_{\text{collisional}}}{S_{\text{radiative}}} \approx \frac{(Z+1.2)E}{800}, \tag{2.1.2.6}$$

where E is the energy of the particle in MeV. By equating the total stopping power components, the critical energy can be approximated as:

$$E_{\text{crit}} \approx \frac{800}{Z+1.2}, \tag{2.1.2.7}$$

where E_{crit} is in MeV. The ratio of the total stopping power components (2.1.2.6) shows that the collisional component dominates in materials with a low atomic numbers Z and at low particle energies. As the particle energy or the atomic number increase, the radiative losses become the dominant form of energy loss.

2.2 $\Delta E - E$ method

The $\Delta E - E$ method is used in multi-layer particle detectors to identify detected particles and measure their total energy. The method is based on the measurement of energy losses of the particle in the detector layers. In the simplest case, the detector consists of an outer detector layer that is thin enough for the particle to go through it and continue to the next detector layer where the particle stops. As the particle passes through the first detector layer, the energy loss of the particle ΔE is measured. The remaining energy E' is deposited in the last detector layer and measured. The sum of the deposited energies $E = \Delta E + E'$ is then the total energy of the particle.

The charge of the particle can be estimated as [13, 14]:

$$Z \approx \left(\frac{k}{L(2+\varepsilon)^{a-1}}\right)^{1/(a+1)} (E^a - E'^a)^{1/(a+1)}, \tag{2.2.0.8}$$

where $E = \Delta E + E'$ is the total energy of the particle, $2+\varepsilon$ is the mass-to -charge ratio of the particle, L is the thickness of the detector layer where the particle deposited the energy ΔE, and k and a are constants that are determined by approximating the range-energy relation in the detector material. In silicon the range-energy relation

can be approximated as [13]:

$$R \approx k \left(\frac{M}{Z^2} \right) \left(\frac{E}{M} \right)^a ,$$

where R and M are the range and mass of the particle, respectively. The value of Z^2M is unique for different nuclides, which form distinctive curves in a ΔE vs. E' plot [14].

In an ideal case with a particle incidence angle of 0°, no statistical fluctuations in the energy-loss process, and an ideal detector, the response tracks of the particles are single curves for different nuclides. Fluctuations of deposited energies in the detector layers are caused, for example, by differences in the incidence angle, variations in the thicknesses of the detector elements, electronic noise, and the statistical nature of the energy-loss process. These fluctuations cause the ideal response tracks to broaden. Figure 2.2 shows simulated response tracks for different energetic ions species in the The Low-Energy Telescope (LET) of the STEREO mission [13]. The vertical axis shows the energy deposited in the penetrated detector layer L1A and the horizontal axis shows the deposited energy in the detector layer L2A, where the particle stops. The left panel shows the actual deposited energies in the detector layers, while the right panel shows deposited energies that have been approximately corrected for variations caused by incidence angle and detector thickness differences [13]. The response tracks of detected particles can be corrected to some degree by calibrating the different detector elements and their electronics individually, and studying the effects of temperature and other external factors on the detector response.

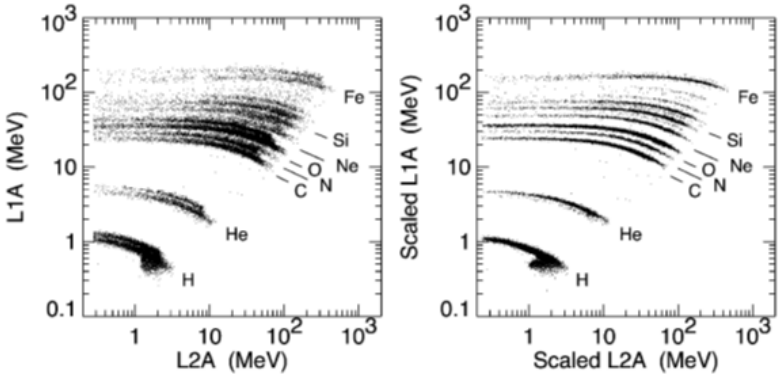

Figure 2.2: Monte Carlo simulated response tracks for different ions species in the LET instrument of the STEREO mission [13]. The deposited energy in the penetrated detector layer (L1A) is shown in the vertical axis and the deposited energy in the detector layer where the particle stops (L2A) is shown in the horizontal axis. The left panel shows the actual deposited energies while the right panel shows energy deposits approximately corrected for variations due to incident angle and detector thickness differences.

2.3 SIXS-P

The scientific goals and requirements, mechanical structure, onboard data handling, and data products of the SIXS-P instrument are covered shortly in this section.

2.3.1 Scientific goals and requirements

The main scientific goal of the SIXS instrument is to make measurements to give accurate estimates for solar X-ray and SEP irradiation at the surface of Mercury. These estimates will enable the MIXS instrument to analyse the fluorescent X-ray emission from the surface of Mercury. The independent scientific objectives of SIXS include: monitoring the temporal variations of the intensity and spectrum of solar X-rays to study the solar corona, monitoring SEP fluxes and energy spectra in the inner heliosphere to study particle acceleration close to the Sun, and measurements of magnetospheric particle fluxes to study Hermean magnetospheric dynamics [9].

SIXS-P will provide long-term data of SEP fluxes near the Sun. These data will give valuable information on the energetic particle transport in the inner heliosphere and on the particle acceleration mechanisms at coronal shocks. The data from SIXS-P can be combined with data from other spacecraft to study coronal and interplanetary particle acceleration and transport [9].

The most abundant particle species that produce fluorescent X-ray emission are

electrons and protons. The trajectories and energies of the particles depend on the magnetic field of the Sun and the Hermean magnetosphere. Due to the non-trivial trajectories of the particles, SIXS-P needs to be able to measure particles with some angular resolution [9]. The different side detector viewing directions provide the needed angular resolution to separate the different directional components of the incoming particle flux. The components are used to determine the flux of particles corresponding to the footprint in the MIXS images.

The proton energy range has to be 1 MeV–30 MeV, which is the energy range where protons are most efficient in producing particle-induced X-ray emission (PIXE). For electrons, the peak PIXE production efficiency is at approximately three times the energy of the observed X-rays. For K-shell ionisation in the elements of interest to the MIXS instrument, the maximum electron energy range is $\sim$2 keV–20 keV [9]. The measurement of electrons at near-relativistic energies ($>$ 100 keV) and both particle types at peak PIXE production rates is impossible with one instrument using only one detection method. The MMO has a particle detector that can measure low-energy electrons and the low-energy electron flux can be indirectly measured from the Bremsstrahlung component of the MIXS instrument observations. For these reasons, the focus of the SIXS-P instrument was chosen to be protons and high-energy electrons. The electron energy range of the instrument should be 0.1 MeV–3 MeV. As the energy range of the particles is broad and the required spectral energy resolution is not very high, a logarithmic spacing is optimal for the energy channels [9].

The SEP precipitation incident on Mercury's surface can occur on the dayside, as well as the nightside of Mercury. SIXS-P will have to be able to measure particle fluxes and directions throughout the MPO orbit, to enable MIXS measurements at any orbital phase [9].

The measured electrons and protons need to be well separated, i.e. the instrument has to be able to identify most particles. Identification of each incident particle is nearly impossible at the lower energies, so there will be some cross-talk between the electron and proton channels.

Based on the time scales of particle flux variability, the time resolution of the instrument does not have to be below 1 min when analysing SEP fluxes. A better

temporal resolution is needed for analysing magnetospheric particle events, so the total counting rate and the counting rates in a couple of energy bands for protons and electrons should be monitored with a time resolution of approximately 1 s [9].

2.3.2 Mechanical structure

The SIXS instrument is built of two separate units: the main electronics unit and the SIXS Sensor Unit (SIXS SU). The main electronics unit contains the Data Processing Unit (DPU), a power supply, interfaces to the SIXS SU, the onboard instrument software, and a SpaceWire interface to the spacecraft. The main electronics unit is shared with the MIXS instrument. The SIXS SU is connected to the main electronics unit with a bundled serial and power cable. The SIXS SU contains the X-ray subdetector SIXS-X and the particle subdetector SIXS-P. The front-end electronics of the subdetectors are also housed in the SIXS SU. Figures 2.3(a) and 2.3(b) show the outer structure and a cross-cut view of the SU.

The SIXS SU outer structure is an aluminium enclosure that resembles a half pyramid with a wall thickness of 3 mm and an extended back wall that works as a heat radiator [16]. The radiator has a saw-cut surface on the anti-sun side to increase the surface area of the radiator. The SU is attached to the spacecraft and thermally isolated from it with thermal stand-offs at the attachment points. All external surfaces that are visible to the Sun or Mercury are covered with an optical solar reflector (OSR) [15, 17] and the surfaces not visible to the Sun or Mercury are covered with a high-emissivity white paint [9]. A picture of the SIXS SU is shown in Figure 2.4.

The particle subdetector is located at the top of the SU. The three X-ray detectors are mounted on the inclined faces of the half pyramid to allow for the necessary field-of-view for the instrument. As shown in Figure 2.3(b), the SIXS SU also contains the main electronics boards for the the subdetectors and the preamplifiers for the X-ray detectors.

The SIXS-P detector head is a multi-layer particle telescope with a cubical arrangement of five 150 μm thick Si side detectors and a CsI(Tl) core scintillator. The side detectors are mounted in five view cones above five of the core scintillator surfaces. The sixth surface (towards the SU) has an epoxy window and a photodiode

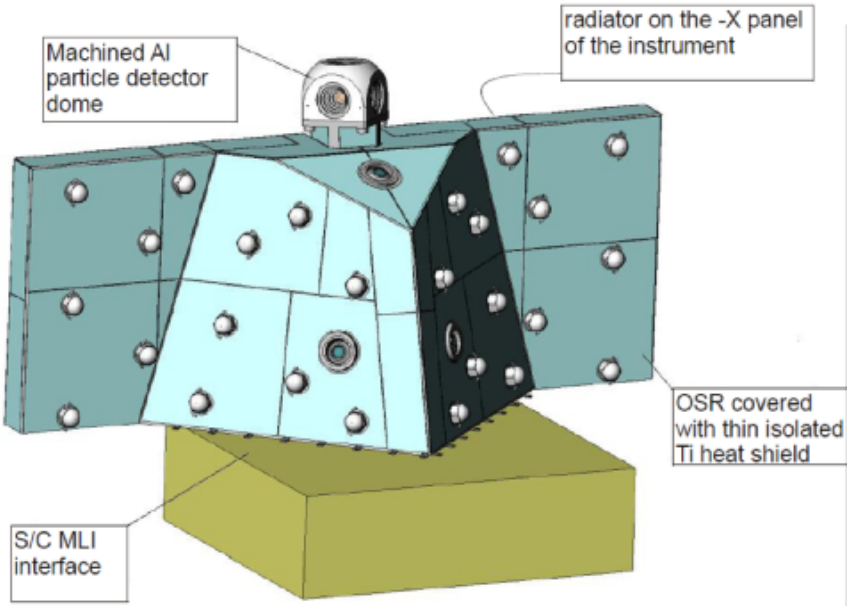

(a) SIXS SU.

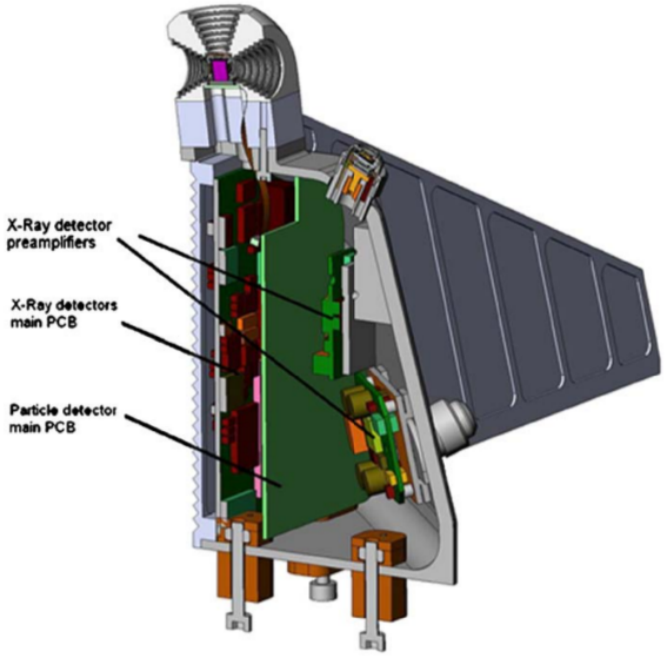

(b) SIXS SU cross-cut.

Figure 2.3: The outer configuration of the SIXS SU [15] is presented in the upper figure and a cross-cut view of the SU [9] is presented in the lower figure. The cross-cut view shows an older triangular version of the back wall radiator and an older orientation of the SIXS-P detector head.

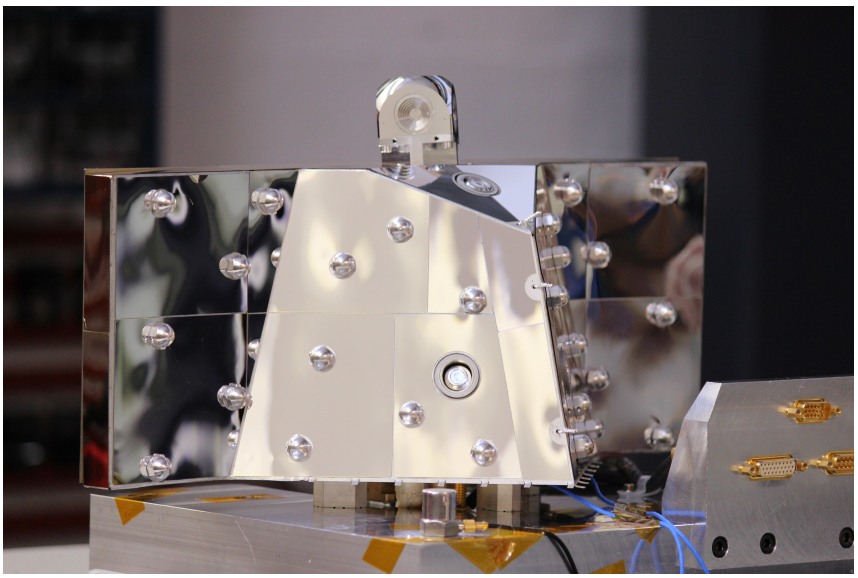

Figure 2.4: Picture of the flight model SIXS SU [18]. The three SIXS-X subdetector windows are visible on the three faces of SU main body. The SIXS-P detector head is visible at the top of the main body.

readout, which records the light output from the scintillator. The dimensions of the core scintillator are $5 \times 5 \times 6.3$ mm^3 and it is designed to stop 30 MeV protons [16]. A cross-cut view of the detector head is presented in Figure 2.5. A picture of the detector head is shown in Figure 2.6.

The detector elements in the detector head are surrounded by a collimator structure, which is designed to stop protons with an energy of approximately 60 MeV [16]. The collimator is an approximately 15 mm thick, roughly hemispherical, aluminium dome with five aperture openings to the side detectors. Each of the openings has collimator rings that limit the angle of the field-of-view of the side detector view cones to 50°. Each of the collimator rings has an outer layer of aluminium and an inner layer of Tungsten. The Al and W layer structure is designed to provide good stopping power while minimising the Bremsstrahlung generated by electrons as they travel in the collimator [16]. One of the side detector view cones is in the anti-nadir direction (side 0) and the others are perpendicular to this direction with an angular separation of 90°[9].

A 5.76 μm thick beryllium foil with a 90 nm layer Vapour Deposited Aluminium (VDA) surface is between the Al and W layers of the lowest collimator ring. A 7.7 μm thick Kapton foil with a 90 nm thick layer of VDA is below the lowest collimator ring, close to the side detector. This configuration is the same for all the side detector

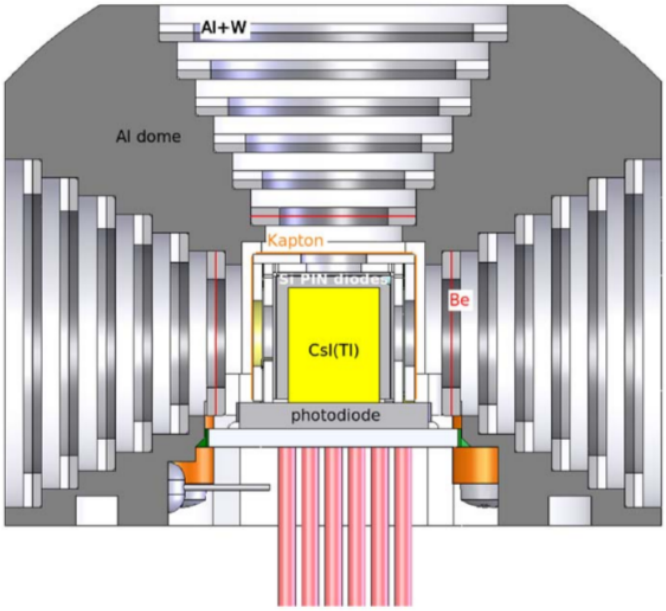

Figure 2.5: A cross section of the SIXS-P detector head [9]. The core CsI(Tl) scintillator is surrounded by the Si side detectors which are in the view cones. The Kapton and Be foils are visible outside the side detectors. The field-of-view of the view cones is limited by the Al + W collimator rings that are mounted on the Al dome. The photodiode is below the core scintillator.

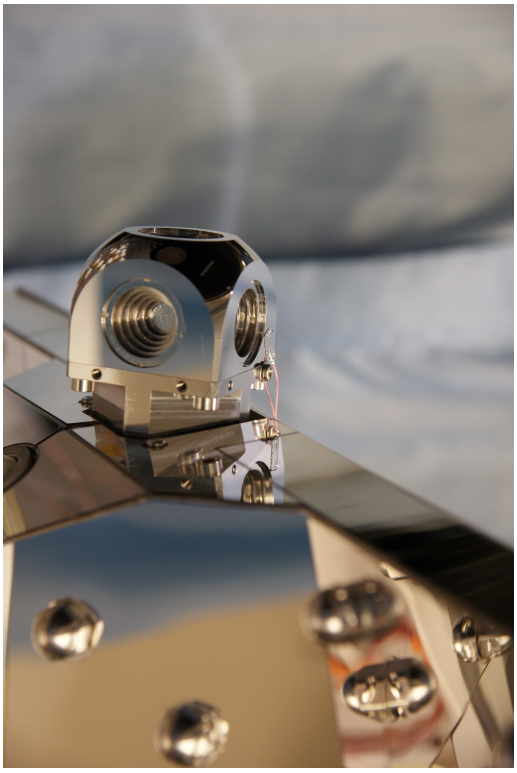

Figure 2.6: A picture of the flight model SIXS-P detector head [18]. The roughly hemispherical shape of the collimator can be clearly seen. The collimator rings and the outer aluminium coating of the beryllium foil are visible in the aperture opening.

view cones, but the actual foil thicknesses vary. The purpose of these foils is to protect the side detectors from the thermal and electromagnetic environment and provide additional shielding from electromagnetic interference. The two foils also provide the side detectors protection from incident optical light [9].

The Si side detectors have two active areas and two passive areas. The centre active area is used to measure the energy loss of the incident particles and the outer active area is used as an anticoincidence (AC) shield. The two active areas are separated by an inner passive area and the outer passive area is located on the edges of the side detector outside the AC active area. The outer active areas of the five side detectors are electrically connected to form one large AC detector around the core scintillator. No event signal is allowed when the AC detector is triggered. The AC detector is used to reduce the background from penetrating particles and to increase the energy resolution by rejecting electrons backscattering from the core scintillator [16].

2.3.3 Data handling

The DPU of SIXS/MIXS processes, analyses and packs the data sent by the SIXS-P measurement electronics to frames suitable for telemetry. The steps in the data processing are [19]:

1. Hit flag logic and raw data buffering
2. Offset correction
3. Reducing the pulse height from a 11-bit value to a 8-bit value by taking a logarithm of the 11-bit value
4. Electronics temperature correction
5. Detector temperature correction
6. Amplification correction
7. Pulse height reducing from 8-bit to 6-bit values with a simple division of the 8-bit values by 4
8. Archiving into the histogram

The particle detector measures the energy loss of the incident particles in the different detector layers. The analogue signals measured from the detector layers are proportional to the energy loss of the particle. The analogue voltages are compared to set threshold values that can be changed during the mission by telecommands. If the measured value is higher than the threshold value, a hit signal is produced for the event and the detector element in question. The registered particle events are converted to digital signals using a 12-bit AD-converter and the least significant bit of the 12-bit ADC value is discarded [20]. The detector has seven different detector elements, whose pulse heights are converted to digital signals:

- five pulse heights corresponding to the Si side detectors (side 0–side 4),
- one core detector pulse height,
- one AC pulse height, which is a sum of all AC elements.

The registered particle events are placed in a raw data buffer from which they are analysed by the DPU's event handler.

An offset correction is applied to the 11-bit pulse heights to take into account the differences in the different side detectors. The offset values are determined by the calibration of the instrument and are presented in section 3.3.

Due to the low energy resolution requirement of the instrument, the 11-bit pulse heights can be truncated to 6-bit logarithmic values [20]. First the 11-bit values are reduced to 8-bit logarithmic values. This can be done with the formula [19]

$$ADC_{8-bit} = 255 \cdot \frac{\ln ADC_{11-bit} - \ln 8}{\ln 2000 - \ln 8}. \qquad (2.3.3.1)$$

The 8-bit ADC values could be corrected for electronics temperature effects, but the effects were observed to be too small to be corrected for. The core scintillator ADC values are temperature corrected according to a pre-defined correction curve based on the measured temperature of the core scintillator.

An amplification correction could be applied at this point of the data processing chain to reduce differences between the gains of the side detector ASIC channels. The amplification correction is not applied in SIXS-P as the effects of the correction were found to be smaller than the resolution of the correction [19].

The 8-bit pulse heights are reduced to 6-bit values and divided into event categories based on the following conditions:

- C1 to C5: Single side events for the different side detectors. Side only events or coincidence events with the core scintillator. For example, events in the C2 category trigger the side 1 detector and possibly the core detector, but not other side detectors or the AC detectors.
- C6: Double hit events. Two particles cause a hit in the same detector element simultaneously.
- C7: Penetrating particles. One side detector, the core scintillator and the opposite side detector are triggered.
- C8: The other hit category. Events that do not fall into the other categories are placed in C8. The instrument does not register particles that hit the AC detectors as events, unless commanded to with a telecommand.

The particle events are then written into an event histogram. The measured protons and electrons are divided into energy channels based on their energy and the triggered hit signals from the different detector elements. The energy channels of the instrument in measured particle energies are:

- Electrons, single detector event. No hit in the core detector:
  - E1: 35–60 keV
  - E2: 60–100 keV
  - E3: 100–180 keV
  - E4: 180–330 keV
- Electrons, coincidence event. Hit in the core detector:
  - E5: 300–1000 keV
  - E6: 1000–3000 keV
  - E7: $>$ 3000 keV
- Protons, single detector event. No hit in the core detector:

  - P1: 0.33–0.50 MeV
  - P2: 0.50–0.70 MeV
  - P3: 0.70–1.50 MeV
  - P4: 1.50–3.00 MeV

- Protons, single detector and coincidence events:
  - P5: 3.0–6.0 MeV

- Protons, coincidence event. Hit in the core detector:
  - P6: 6–10 MeV
  - P7: 10–17 MeV
  - P8: 17–30 MeV
  - P9: $>$ 30 MeV

This division of particle events (categories C1–C5) into the energy channels (i.e. extraction of spectral information from the event histogram) is done with a lookup table. The lookup table can be updated during the mission by sending the instrument a telecommand. The lookup table is a 64×64 matrix indexed by the side detector 6-bit pulse height and the core detector 6-bit pulse height. The zeroth column of the side detector values is reserved for events where the core detector was not triggered (single detector events). The elements in the matrix are assigned to the different energy channels. A measured particle belongs to the energy channel whose element indices correspond to the 6-bit side and core detector pulse heights. In Figure 2.7, a particle has been detected with a side detector 6-bit pulse height of 3 and a core detector 6-bit pulse height of 6. The energy channel of the particle can now be determined by comparing the 6-bit pulse heights and the corresponding cell in the lookup table. Based on the example lookup table in Figure 2.7, the particle belongs to energy channel E5. The method of creating the lookup table, and the created lookup table is presented in chapter 4.

In SIXS's normal operating mode (SCIENCE mode), the particle science telemetry consists of [20]:

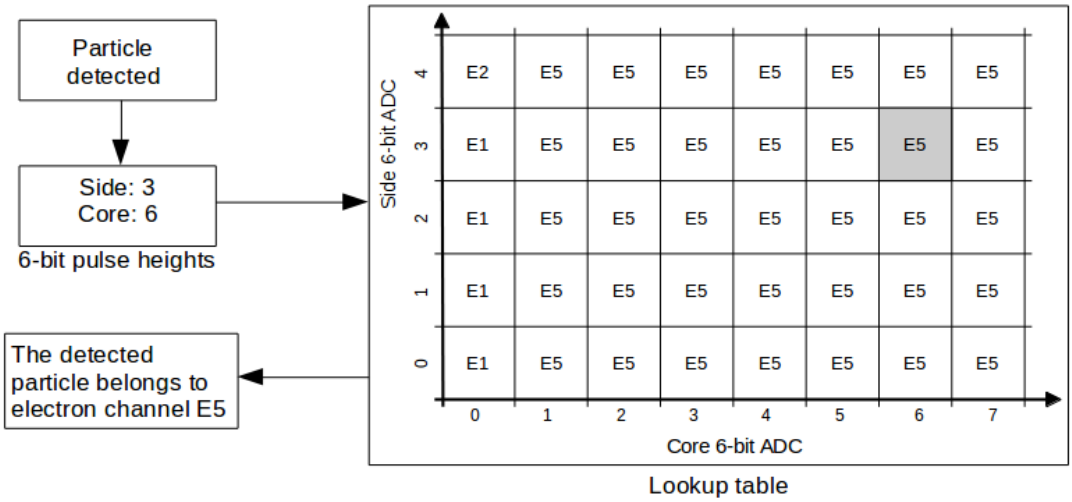

Figure 2.7: Identification of a detected particle with the lookup table. The detected particle causes a side detector 6-bit pulse height of 3 and a core detector 6-bit pulse height of 6. The 6-bit pulse heights are compared with the corresponding cell in the lookup table, and the particle has been identified to belong to energy channel E5.

- Energy spectrum of protons divided into nine energy channels, using the lookup table. The spectrum is sampled separately for all five viewing directions with an 8 second time resolution.
- Energy spectrum of electrons divided into seven energy channels, using the lookup table. The spectrum is sampled separately for all five viewing directions with an 8 second time resolution.
- Up to 16 sample raw data particle events per 64 seconds.
- Particle counting rates in two proton and two electron flux channels, sampled with a 1 second time resolution.
- Four error counters with an 8 second time resolution. The error counters are: spectral error counter, double-hit counter, penetrating particle counter and other event counter.
- Serial-line throughput per one thousand of instrument integration time, with a one second time resolution.
- Dead time of the instrument per one thousand of instrument integration time, with a one second time resolution.

The flux channels for protons and electrons are chosen from the energy channels of the instrument. The flux channels should be as clean as possible, i.e. the proton flux channels should be the channels least contaminated by electrons and vice versa.

2.4 Calibration method

The SIXS-P instrument has to be calibrated so that the ADC values from the instrument can be converted into energy values. Also the differences in the side detectors have to be calibrated, so that the events from the different side detectors are comparable.

If the detector is used to measure electrons and protons of known incident energies, the ADC values from the instrument in addition to simulation data can be used to calibrate the instrument. The energy deposited by a particle in a detector segment can be simulated with the Geant4 software. The Geant4 software and the methods to simulate the deposited energies are presented in chapter 3. If the same particle energy and incident angle is used in experimental measurements and simulations, the ADC values in the detector segments will approximately correspond to the energy loss of a particle in the same detector segments in the simulations. A calibration curve can be fitted to the discrete experimental ADC values and simulated energy losses to produce a continuous correspondence between energy loss and ADC values in the different detector segments.

If the experimental measurements are done with all of the different side detectors, the calibration can be done to all the side detectors separately. In an ideal case, the side detectors are identical and the calibration parameters are the same. Due to the small differences in the side detectors (electronics etc.) the calibration parameters will be slightly different for the different side detectors. The side detectors can be calibrated using events, where the particle stops in the side detector (side only events), and the core scintillator with events where the particle penetrates the side detector and stops in the core scintillator (side + core events).

3 Calibration and particle response simulations

Geant4 software was used to calibrate and simulate the particle response of the SIXS-P subdetector. The Geant4 software is described shortly in the first section of this chapter. The simulation model of the SIXS-P that was used in the Geant4 software is described in the section 3.2. The energy response calibration method and calibration results are presented for protons and electrons in section 3.3. Section 3.4 describes the method and results of SIXS-P subdetector's simulated particle response to a flat energy spectrum of protons and electrons. The simulated particle response of SIXS-P to cosmic rays is presented in the last section of this chapter.

3.1 Geant4 software

The Geant4 software is a free simulation toolkit for simulating passage of particles through matter using Monte Carlo methods. The toolkit was designed and developed by a large international collaboration consisting of physicists and software engineers from research laboratories, national institutes, universities, and high-energy physics experiments [21]. The toolkit source code, documentation, tutorials, and examples are available at the Geant4 collaborations website[1]. Geant4 can be used to create and track particles, visualise particle tracks, design and implement complex geometries for particle detectors and environments, as well as provide simulations for a large variety of physics processes and models in a high energy range (250 eV–1 PeV) [21]. The physics processes implemented in Geant4 cover, for example, electromagnetic, hadronic and optical processes.

The software is the successor of the Geant3 software created at the European Organization for Nuclear Research (CERN). Unlike Geant3 which was written in the FORTRAN programming language, Geant4 is written in the C++ programming language with an object-oriented approach. Due to its objected-oriented implemen-

[1] `https://geant4.web.cern.ch/geant4/`, accessed: July 2016

tation, Geant4 is modular and easily extendable by the user. The toolkit is used in various fields, such as high-energy physics, medical physics, radiation protection, space physics and space instrumentation, nuclear physics, and particle physics [21].

An updated version of the SIXS-P simulation model was used in the Geant4 simulations presented in this thesis.

3.2 SIXS-P simulation model

The SIXS-P simulation model is a Geant4 model that describes the mechanical model of the detector and the needed physical processes. The model was built by ASRO with Geant version 4.9.2.02p. The mechanical model is mainly based on a CAD model of SIXS-P. The model described in [22] was updated with more realistic foil and side detector thicknesses.

3.2.1 Mechanical model

The instrument consists of six separate detectors and support structures. The thicknesses and materials along the X axis and along the Z axis are presented in Tables 3.1 and 3.2, respectively. The model has five silicon side detectors and a CsI(Tl) core detector. The core detector is a solid block of CsI with a size of $6.3 \times 5.0 \times 5.0$ mm^3. A silicon photodiode with an active area of 5.0×5.0 mm^2 and thickness of 380 μm is located under the core detector. As in the real detector, an epoxy window and glue are between the photodiode and the core detector. The window and glue are modelled as a solid epoxy layer with a thickness of 100 μm.

The five Si side detectors are located above the five surfaces of the core detector without the photodiode. The side detectors have two active areas and two passive areas. The centre active area is used to measure the deposited particle energy and the outer active area is used as an anticoincidence (AC) shield. The circular centre active area with a diameter of 2.5 mm is below the opening of the collimator rings. The outer active area is separated from the centre active area by a 450 μm wide passive ring. The second passive area is outside the outer active area on the edges of the side detector. The configuration of the side detectors is presented in figure 3.1. The top and bottom side of the 157.8 μm thick Si side detectors have dead layers of

Table 3.1: Thicknesses and materials of layers along the X axis. Layers are in order from top side opening (Side 0) to bottom of the instrument.

Layer name	Thickness [μm]	Material
Outer foil surface	0.1	Al
Outer foil	5.76	Be
Space between layers	2090	Vacuum
Inner foil surface	0.1	Al
Inner foil	7.6	Kapton
Space between layers	1000	Vacuum
Side detector dead layer (top)	0.6	Si
Side detector active layer	157.8	Si
Side detector dead layer (bottom)	0.67	Si
Space between layers	650	Vacuum
Core surface	1	CsI
Core detector	6299	CsI
Epoxy window and glue	100	Epoxy
Photodiode	70	Si
Photodiode package	1240	Alumina
Cross plate	1000	Kapton

Table 3.2: Thicknesses and materials of layers along the Z axis. Layers are in order from one side opening to opposite side opening.

Layer name	Thickness [μm]	Material
Outer foil surface	0.1	Al
Outer foil	5.76	Be
Space between layers	1990	Vacuum
Inner foil surface	0.1	Al
Inner foil	7.6	Kapton
Space between layers	1100	Vacuum
Side detector dead layer (top)	0.6	Si
Side detector active layer	157.8	Si
Side detector dead layer (bottom)	0.67	Si
Space between layers	650	Vacuum
Core surface	1	CsI
Core detector	4988	CsI
Core surface	1	CsI
Space between layers	650	Vacuum
Side detector dead layer (bottom)	0.67	Si
Side detector active layer	157.8	Si
Side detector dead layer (top)	0.6	Si
Space between layers	1100	Vacuum
Inner foil	7.7	Kapton
Inner foil surface	0.1	Al
Space between layers	1990	Vacuum
Outer foil	5.76	Be
Outer foil surface	0.001	Al

Si with thicknesses of 0.6 μm and 0.67 μm.

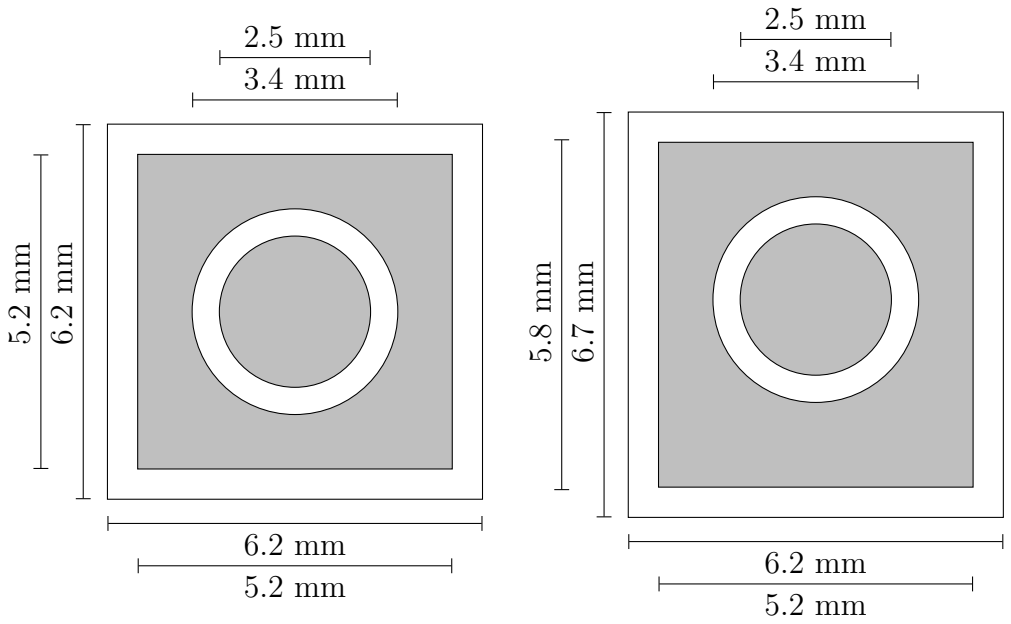

Figure 3.1: The dimensions of the top side detector on the left, and other side detectors on the right. Grey areas are the active parts of the detector, and white areas are the passive areas.

The supporting structures consist of a collimator, two supporting cages, foils and a cross plate PCB (Printed Circuit Board). The roughly hemispheric aluminium (RSA-6061) collimator, with five apertures, forms the outer structure of the detector. Collimator rings inside all of the five apertures reduce the solid angle seen by the detector. Each collimator ring is made of an outer layer of aluminium and an inner layer of tungsten. Both layers are 0.5 mm thick.

Two supporting cages of 0.5 mm thick alumina are between the collimator and the side detector. The openings in the two cages are 3.0 mm and 2.68 mm, respectively.

A 5.76 μm thick beryllium foil with a 0.1 μm thick aluminium surface is attached between the layers of the lowest collimator ring. A 7.6 μm thick Kapton foil with a 0.1 μm surface of aluminium is above the outer cage structure.

The detectors and cages are on the cross plate, and the cross plate PCB is fixed to the collimator. The cross plate PCB is modelled as a 13.6×13.6 mm^2 Kapton square with a thickness of 1 mm.

3.2.2 Physical processes in the model

The tracking of particles in Geant4 is controlled by physical processes. Multiple physics processes are available to model different particle interactions and physical phenomena. The user can choose the processes best suited for the simulation. The low energy electromagnetic physics list G4EmPenelopePhysics is used in the model, and hadronic processes are modelled with G4HadronElasticPhysics and HadronPhysicsLHEP physics lists.

The simulated particles are transported step by step in the simulation volume and tracked until they stop or leave the simulation volume. The steps are implemented with a tolerance, which allows optimisation of the computation performance and preserves required tracking precision [21]. Each used physical process proposes a step to the simulated particle and the program's tracking category implements the most suitable of these steps. Tracks of ten normally incident electrons and protons in a stack of detector elements are shown in Figure 3.2. The shown detector elements correspond in material, thickness, and spacing to those of the side 0 configuration of the SIXS-P Geant4 model. The differences in passage of electrons and proton in matter are clearly visible in the figure. Electrons scatter with large angles, even backwards, and produce secondary particles, while protons go through matter with little change in direction and stop at almost the same point. Figure 3.2 was produced with SPENVIS MULASSIS software[2], which uses the Geant4 transportation and tracking categories.

Particle cut-off values are used to determine which secondary particles are registered. If a secondary particle has a range higher than the cut-off range, the particle is registered and modelled. If the range is shorter than the cut-off range, the energy of the secondary particle is deposited in the current step. The used range cut-off values for gamma rays, protons, and electrons are 10 μm.

The core scintillator's light yield is not simulated in the model. In Geant4, the user is required to input optical parameters, which are difficult to obtain accurately enough [22]. A simple model was used to study the photon detection efficiency as a function of incidence angle. The study is presented as an appendix in [22]. The study showed that the photon detection efficiency is approximately 10 % lower when

[2] `https://www.spenvis.oma.be/`, accessed: July 2016

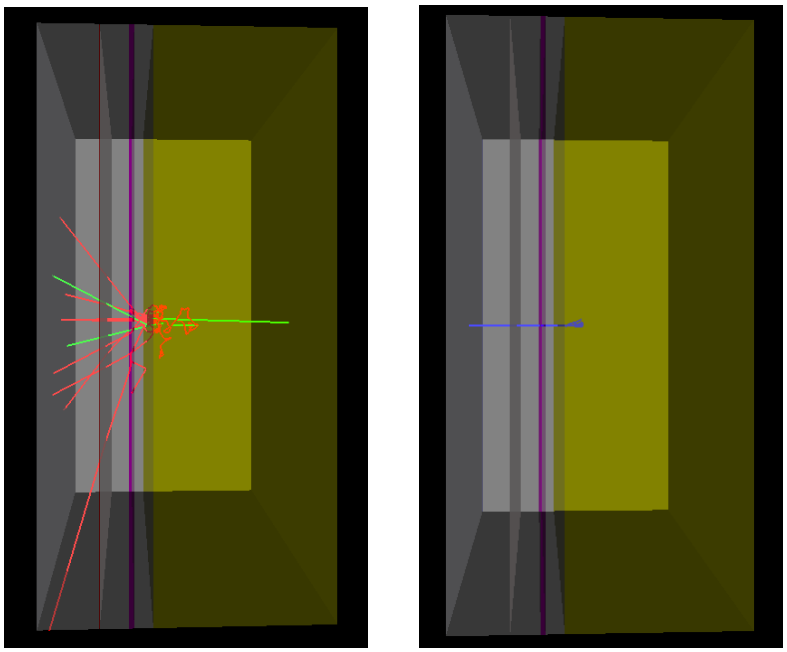

(a) 1.5 MeV electrons. (b) 15 MeV protons.

Figure 3.2: Tracks of ten 1.5 MeV electrons and ten 15 MeV protons simulated with SPENVIS MULASSIS. The particles enter the detector from the left, which corresponds to side 0 of the SIXS-P instrument in material, thickness, and spacing of the detector elements. The detector elements from left to right are: beryllium foil, kapton foil, side Si detector (purple), and core CsI scintillator (yellow). Red particle tracks are electrons, green are secondary particles from the electrons, and blue are protons.

protons ($E < 10$ MeV) or electrons ($E < 500$ keV) come through the top side Si detector. The study also showed that small changes in the optical parameters and the glue or photodiode window thicknesses can cause a 10 % to 20 % error in the photon detection efficiency [22].

3.3 Energy response calibration

Energy losses in the detector layers and ADC values were calibrated for protons and electrons with perpendicular events. The energy losses in side and core detectors were simulated with the Geant4 software and compared with experimental ADC values from proton [19] and electron measurements [23].

3.3.1 Simulation set-up

A particle beam was simulated with the Geant4 software from a 20 mm diameter circular plane source, placed at (17.9 mm, 0 mm, 0 mm). Beam1d angular distribu-

tion with a 3 degree sigma value was used to simulate the angular distribution of the beam. The simulated particles were produced with a Gaussian energy distribution. A sigma value of 2 keV was used for the energy distribution. The direction of the beam was towards the negative X axis (-1, 0, 0).

The particle energies were chosen to match the measured experimental beam energies in the proton and electron measurements. 1 000 000 particles were simulated for each incident energy.

One side detector can be used to simulate the energy responses of all the side detectors, as the side detectors are identical in the simulation model and the effect of the core scintillator geometry was found to be negligible. The incident particles hit side 0 detector in the simulations.

Histograms of the deposited energies in the side and core detector were created from the Geant4 output files for each beam energy and a normal distribution was fitted to the energy peaks in the histograms. The locations of the energy peaks in the side and core detectors were used as the energy losses for each beam energy respectively. Example energy peaks in the side and core detectors for a 17.58 MeV proton are presented in Figures 3.3(a) and 3.3(b).

3.3.2 Proton events

The energy losses as a function of the ADC values, and ADC values as a function of energy losses were plotted. Core detector data points with an ADC value ≤ 1024 were used to avoid effects caused by the saturation of the AD converter when ADC values approach a value of 2048. A linear function

$$y = A + Bx \tag{3.3.2.1}$$

was fitted to the side detector data and a power-law function

$$y = A' + B'x^{C'} \tag{3.3.2.2}$$

was fitted to the core detector data for both E(ADC) and ADC(E) cases. The process was repeated separately for measurements of all of the side detectors. An example fit of Side 0 ADC(E) side calibration is presented in Figure 3.4. An example

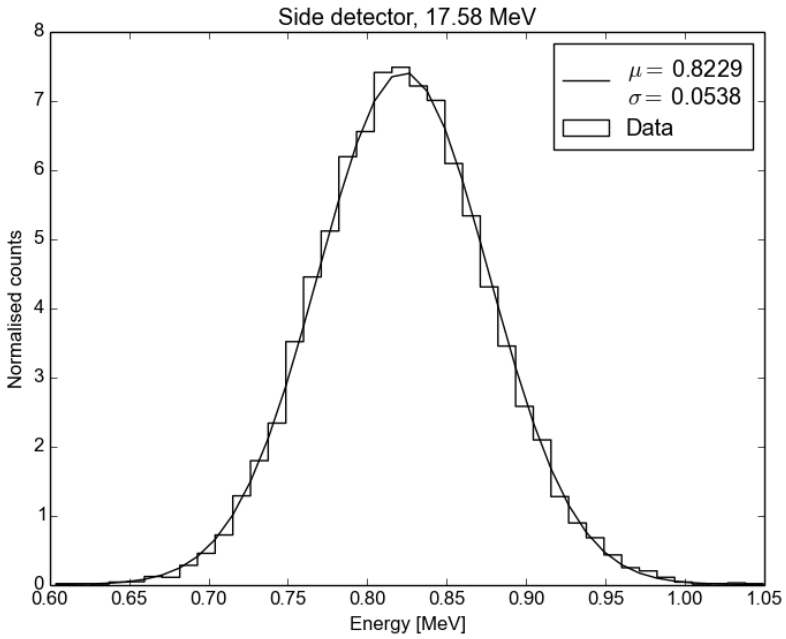

(a) Energy loss in the side detector.

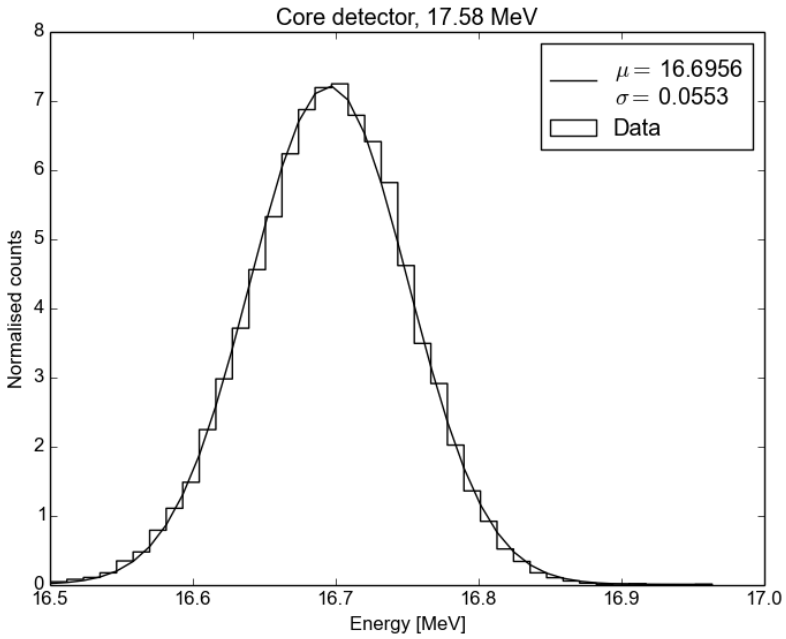

(b) Energy loss in the core detector.

Figure 3.3: Energy loss of a 17.58 MeV proton in the Side Si detector and in the CsI core scintillator. The location of the side detector energy peak is at 0.8229 MeV and the core detector energy peak is at 16.6956 MeV.

core calibration for the same side detector is presented in Figure 3.5. The amount of data points varies by side detector, due to the experimental data.

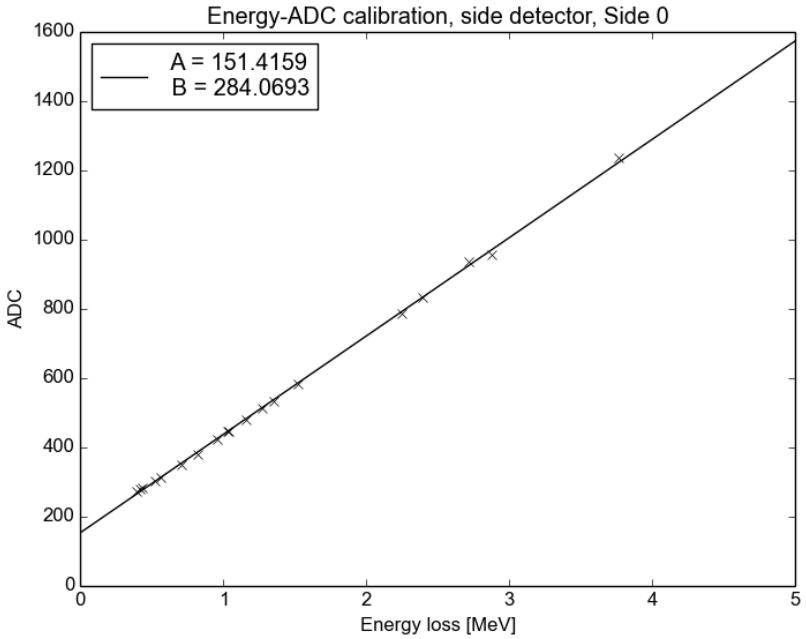

Figure 3.4: Proton ADC(E) side calibration using Side 0 data.

3.3.3 Electrons events

The electron events were analysed in the same way as the proton events. Due to the small number of electron core events, the electron core calibration was omitted. An example fit of Side 1 ADC(E) side calibration is presented in Figure 3.6.

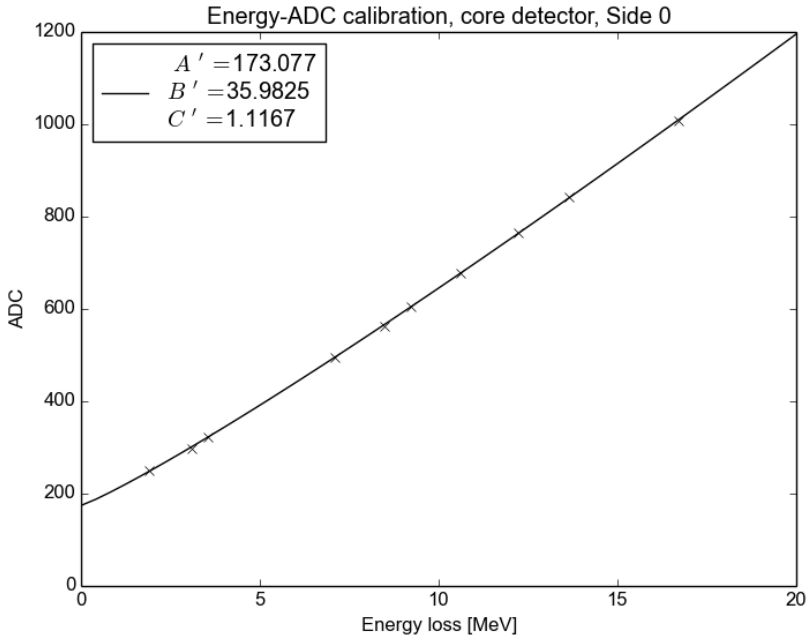

Figure 3.5: Proton ADC(E) core calibration using Side 0 data.

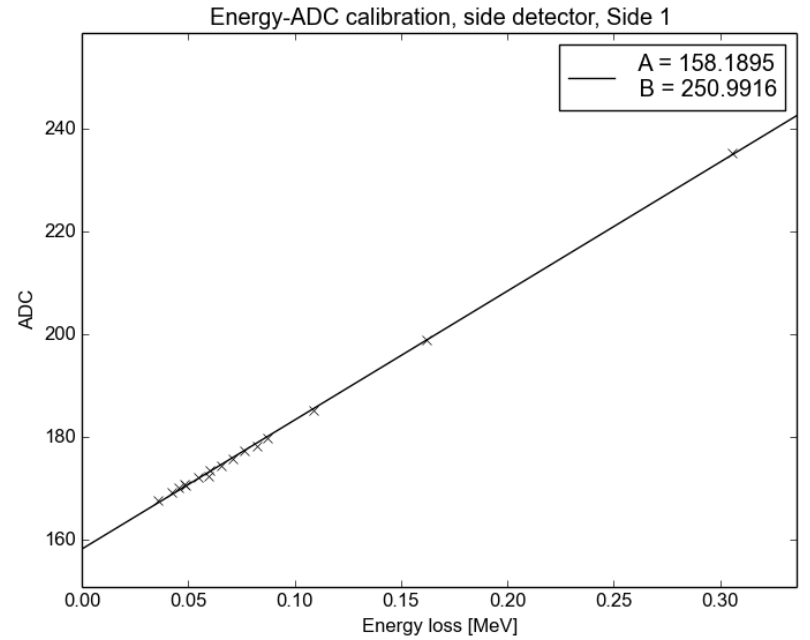

Figure 3.6: Electron ADC(E) side calibration using Side 1 data.

3.3.4 Results

3.3.4.1 Protons

The fitting parameters for the proton ADC(E) and the E(ADC) side and core calibrations are presented in Tables 3.3 and 3.4. The proton ADC(E) side and core calibration curves for different side detector events are presented in Figures 3.7 and 3.8. The side detector energy response to protons is linear and the core energy response to protons is non-linear.

Table 3.3: Proton side detector calibration parameters for ADC(E) and E(ADC).

	ADC(E)		E(ADC)	
Side	A [ch]	B [ch/MeV]	A [MeV]	B [MeV/ch]
0	151.416	284.069	-0.531849	0.00351810
1	138.757	286.196	-0.484115	0.00349285
2	153.346	284.543	-0.537236	0.00351168
3	147.083	286.994	-0.511754	0.00348309
4	154.024	288.152	-0.533314	0.00346829

Table 3.4: Proton core detector calibration parameters for ADC(E) and E(ADC).

	ADC(E)			E(ADC)		
Side	A' [ch]	B' [ch/MeV]	C'	A' [MeV]	B' [MeV/ch]	C'
0	173.077	35.9825	1.11674	-4.59125	0.0631124	0.841680
1	169.985	36.6891	1.09818	-4.46409	0.0551222	0.864175
2	166.800	39.0644	1.07935	-4.15169	0.0455959	0.888973
3	178.789	34.2343	1.11965	-4.87392	0.0657353	0.841207
4	170.180	36.5909	1.10012	-4.40983	0.0543068	0.865676

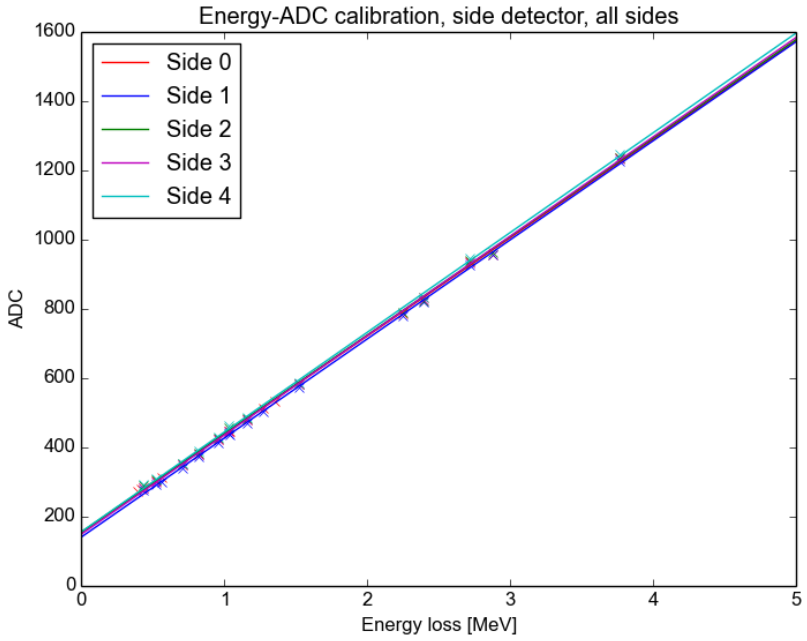

Figure 3.7: Proton ADC(E) side calibration curves for different side detectors.

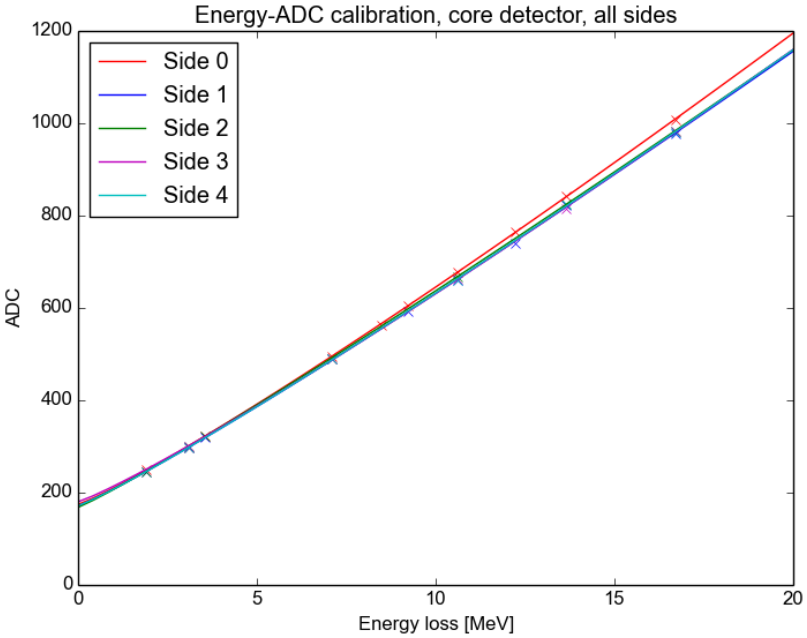

Figure 3.8: Proton ADC(E) core calibration curves with data for different sides.

3.3.4.2 Electrons

The fitting parameters for the electron ADC(E) and E(ADC) side calibrations are presented in Table 3.5. The electron ADC(E) side calibration curves for different side detector events are presented in Figure 3.9. The side detector electron energy response of the SIXS-P detector is linear.

Table 3.5: Electron side detector calibration parameters for ADC(E) and E(ADC).

	ADC(E)		E(ADC)	
Side	A [ch]	B [ch/MeV]	A [MeV]	B [MeV/ch]
0	167.513	243.464	-0.686243	0.00409755
1	158.190	250.992	-0.629841	0.00398187
2	172.329	253.015	-0.680531	0.00394940
3	165.407	252.194	-0.655199	0.00396161
4	173.593	253.492	-0.684585	0.00394377

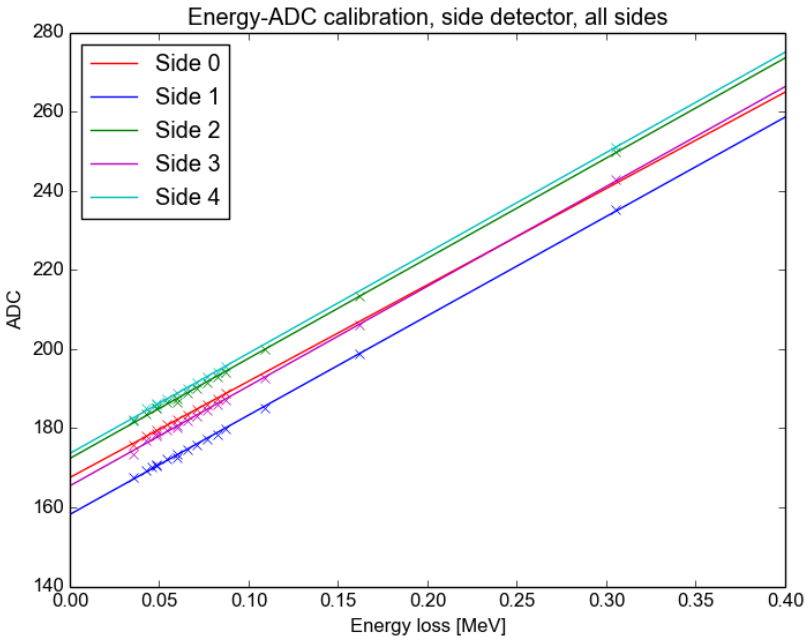

Figure 3.9: Electron ADC(E) side calibration curves for the side detectors.

3.4 Acceptance of the SIXS-P detector

The acceptance of the SIXS-P detector was analysed for protons and electrons. The energy losses of an isotropic particle flux with a linear energy distribution were simulated with the Geant4 software.

3.4.1 Acceptance of a particle detector

The isotropic flux of a particle type i detected by a particle detector is:

$$F_i = \frac{C_i}{A_i}, \tag{3.4.1.1}$$

where F_i is the flux of the identified particle i in units $\mathrm{cm}^{-2} \cdot \mathrm{sr}^{-1} \cdot \mathrm{s}^{-1}$, C_i is the detector counting rate of particle type i in units s^{-1}, and A_i is the acceptance of the detector in units $\mathrm{cm}^2 \cdot$ sr [24]. The acceptance of the detector describes the ability of a particle detector to detect particles of a certain type and energy from its field-of-view. Acceptance can be defined as:

$$A_i = GF \cdot \eta_i, \tag{3.4.1.2}$$

where GF is the geometric factor of the detector in units $\mathrm{cm}^2 \cdot$ sr, and η_i is the efficiency of the detector to detect and identify particles incident on the detector [24].

3.4.2 Simulation set-up

The simulation geometry consisted of the SIXS-P detector model with five rectangular particle sources placed at (17.9, 0.0, 0.0) mm, (3.7, -17.9, 0.0) mm, (3.7, 17.9, 0.0) mm, (3.7, 0.0, -17.9) mm and (3.7, 0.0, 17.9) mm. The source in the YZ plane was 35.8 mm in the Y direction and 35.8 mm in the Z direction. The other sources were 28.4 mm in the X direction and 35.8 mm in the Y/Z direction. The sources in the XY and XZ planes were moved in the positive X direction in order to align them with the collimator dome.

The angular distribution of the sources was a $\cos^2\theta$ distribution with $\theta \in [0°, 60°]$. A $\cos^2\theta$ distribution with $\theta \in [0°, 90°]$ represents a distribution seen at a plane from a 2π sr isotropic flux. The energy distribution of the particles was uniform with energies between 0.8 MeV and 100.0 MeV for protons, and between 0.04 MeV and 6.0 MeV for electrons.

The used simulation geometry with rectangular particle sources was chosen, instead of a hemispheric particle source enclosing the whole detector dome, to reduce run time in the simulations. The simulation was run with 200 000 000 particles

for both protons and electrons respectively. 2 641 339 proton events and 1 700 113 electron events were recorded out of the 200 000 000 generated particles.

3.4.3 Data analysis

The output data of the simulation was divided into event categories (C1–C5,C7,C8) and the event categories into energy channels. The used event categories mimic the event categories used in the real instrument. Energy losses in the active areas of the detector were used to separate the events into the event categories.

Category C6 (double hits) is not used in the simulations, as the simulated particles are generated one at the time. In the simulations, the AC hits are registered in the C8 category, unlike in the real instrument where they are not registered as events unless specifically instructed with a telecommand.

If the energy loss in a detector is greater than the set threshold energy for that detector, the particle triggers that detector. The used thresholds were 30 keV for the side detectors, 300 keV for the core scintillator, and 100 keV for the anticoincidence detectors. The sum of energy losses in all the AC detectors caused by a single particle was compared with the AC threshold, as the AC detectors are electrically connected in the real instrument and the ADC is read as a single value.

The number of events and the relative number of events in each category is presented in Table 3.6.

Table 3.6: Number and fraction of simulated particle events in different event categories.

	Protons		Electrons	
Category	No.	Fraction	No.	Fraction
C1	81178	0.0307	77369	0.0455
C2	85828	0.0325	88291	0.0519
C3	85951	0.0325	88897	0.0523
C4	85823	0.0325	89191	0.0525
C5	85812	0.0325	88961	0.0523
C7	6108	0.0023	1481	0.0009
C8	2210639	0.8369	1265923	0.7446

The simulated particle events in the event categories were divided into energy channels using the detected energies. If the sum of the energy losses in the side detectors and the core detector was greater than or equal to the lower limit of the channel and less than the upper limit of the channel, the event was placed in that

energy channel. A histogram of incident energy values in each energy channel was created for protons and electrons respectively.

The geometric factor of the particle source is:

$$GF = A\pi(1 - \cos^2\theta_{\max}) \tag{3.4.3.1}$$

$$= \left((3.58\text{ cm})^2 + 4 \cdot (2.84\text{ cm} \cdot 3.58\text{ cm})\right) \cdot \pi \cdot (1 - \cos^2 60^\circ) \tag{3.4.3.2}$$

$$\approx 126.0\text{ cm}^2 \cdot \text{sr}, \tag{3.4.3.3}$$

where A is the area of the particle source and $\theta_{\max}$ is the maximum angle of the used $\cos^2\theta$ distribution. The normalisation factor is then:

$$G = GF \cdot \frac{1}{N_{\text{chan}}} \tag{3.4.3.4}$$

$$= GF \cdot \frac{E_{\max} - E_{\min}}{\Delta E \cdot N_{\text{source}}}, \tag{3.4.3.5}$$

where N_{chan} is the number of particles created from the source with energies belonging to bin ΔE, N_{source} is the total number of created particles from the source, $E_{\max}$ and $E_{\min}$ are the upper and lower limits of the used energy distribution, and ΔE is the width of the histogram bin. The unit of the normalisation factor is then $\frac{\text{cm}^2 \cdot \text{sr}}{\text{particles}}$. By multiplying the number of particles in a histogram bin with the corresponding normalisation factor G, we get a normalised particle count i.e. the acceptance in units cm$^2\cdot$ sr.

The histogram count in each bin was multiplied with the normalisation factor G and plotted as a function of incident energy.

3.4.4 Results

Acceptance to protons as a function of particle energy in event categories C1–C5, C7 and C8 in proton energy channels is presented in Figure 3.10. Acceptance to protons as a function of particle energy in event categories C1–C5 in proton energy channels is presented in Figure 3.11.

The proton energy channels are clean in the nominal energy range. Protons with energies over 20 MeV start to produce non-ideal response in the lower energy channels. Protons with energies above approximately 40 MeV produce non-ideal

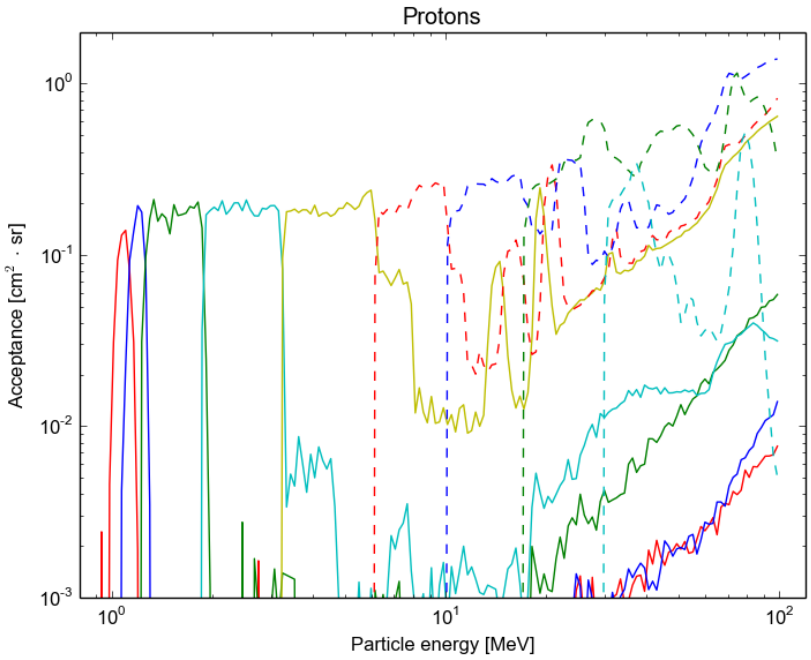

Figure 3.10: Acceptance to protons in proton energy channels. Proton channels P1–P9 are in ascending order from left to right. All event categories included in the data.

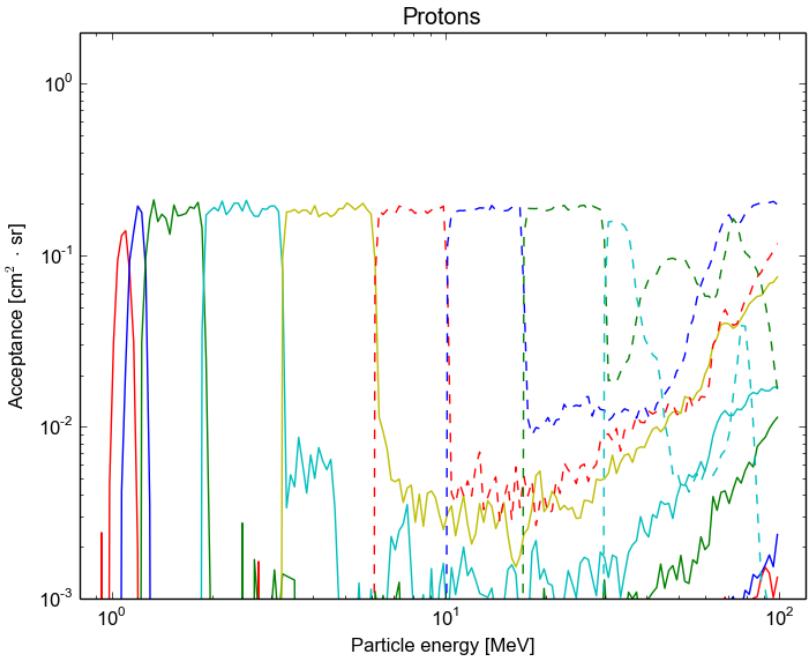

Figure 3.11: Acceptance to protons in proton energy channels, using event categories C1–C5. Proton channels P1–P9 are in ascending order from left to right.

response in all proton channels apart from P9.

Acceptance to electrons as a function of particle energy in event categories C1–C5, C7 and C8 in electron energy channels is presented in Figure 3.12. Acceptance to electrons in event categories C1–C5 in electron energy channel is presented in Figure 3.13.

The electron channels are clean in the nominal energy range apart from channels E6 and E7. E6 measures approximately as much, or more, electrons of energies belonging to channel E7. This is likely due to the characteristic complex scattering of the electrons which causes some of the electrons to scatter out of the detector, and Bremsstrahlung, which causes energy to exit the detector undetected.

The division of particle events into particle categories cleans the energy channels, as visible when comparing the C1–C5 (Figures 3.11 and 3.13) and C1–C8 plots (Figures 3.10 and 3.12).

The determined electron and proton acceptances exhibit a fairly high amount of statistical fluctuations, especially in the lower energy region of the simulation runs, due to a fairly low amount of simulated particles for a flat spectrum that has been divided into logarithmic bins. This can be mitigated by simulating mono-energetic particles at pre-defined energy values instead of using a flat energy spectrum.

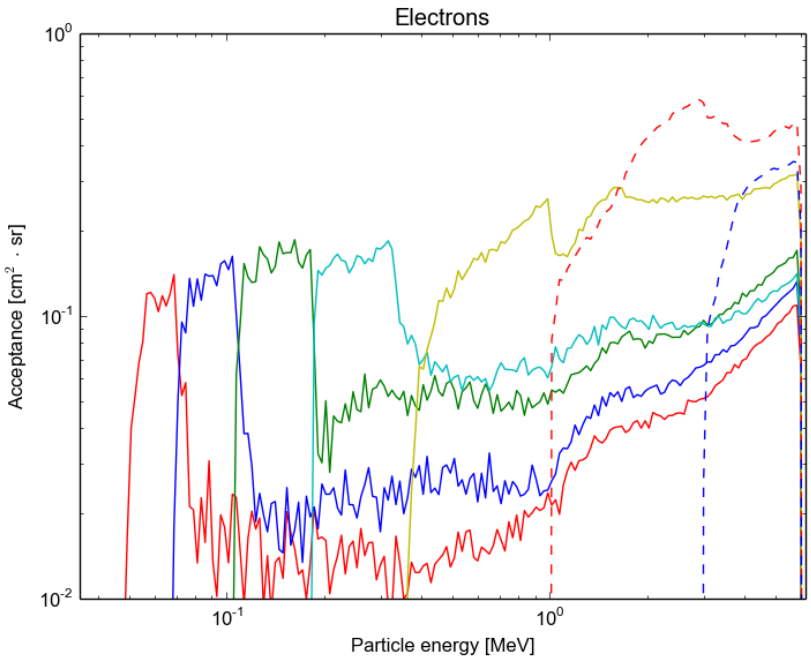

Figure 3.12: Acceptance to electrons in electron energy channels. Electron channels E1–E7 are in ascending order from left to right. All event categories included in the data.

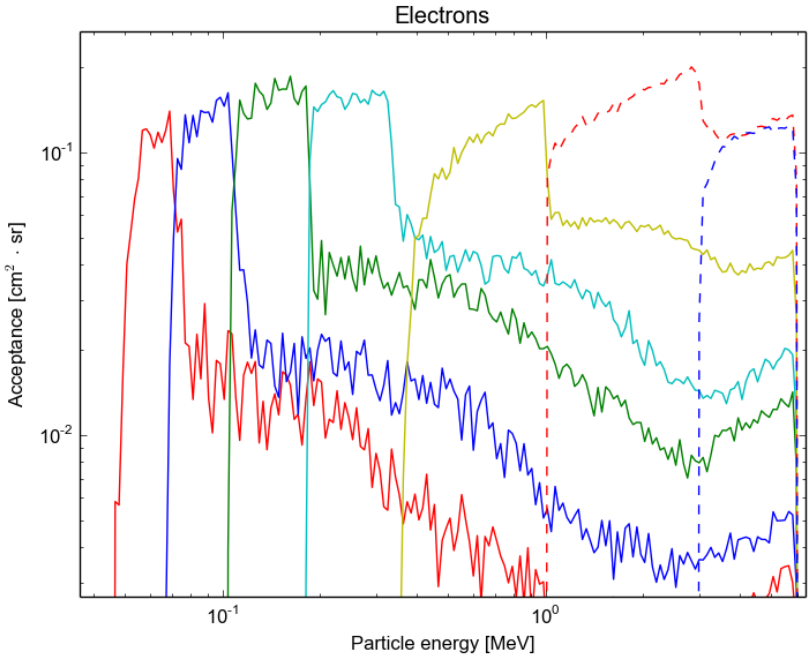

Figure 3.13: Acceptance to electrons in the electron energy channels, using event categories C1–C5. Electron channels E1–E7 are in ascending order from left to right.

3.5 Cosmic ray proton and quiet time electron response of the SIXS-P detector

The cosmic ray proton response and the quiet time electron response of the detector were simulated using cosmic ray proton and electron quiet time spectra from literature.

3.5.1 Simulation set-up

The used simulation geometry and angular distribution were identical to the simulation set-up of the acceptance simulations presented in section 3.4.2. The simulation set-up is not optimal for cosmic ray protons, as high energy protons pass through the collimator. For this reason, the simulated response to cosmic protons should be regarded as an approximative result. The energy distributions were input to Geant4 as user generated intensity histograms separately for protons and electrons. 160 000 000 protons and 80 000 000 electrons were created in the simulation.

3.5.2 Cosmic ray protons

The used cosmic ray proton spectrum was

$$J_{LIS}(T) = \frac{1.9 \cdot 10^4 \cdot P(T)^{-2.78}}{1 + 0.4866 \cdot P(T)^{-2.51}}, \tag{3.5.2.1}$$

where $P(T) = \sqrt{T(T + 2T_r)}$, J and T are expressed in units of particles/(m^2 · sr · s · GeV) and in GeV, respectively, and $T_r = 0.938$ GeV [25].

The energy limits were calculated so that the energy range contains approximately 90 % of the total particle flux. A histogram of intensity was created between 10 MeV and 1641 MeV, and used in the Geant4 macro file to produce particles with the desired energy distribution.

3.5.3 Quiet time Jovian electrons

The quiet time electron spectrum is the spectrum of electrons during periods with quiet solar activity, dominated by Jovian electrons. Jovian electrons are electrons that have been accelerated in Jupiter's magnetosphere and propagated along magnetic field lines in the heliosphere. Jovian electrons are the dominant electron population in the heliosphere during times without sudden short timescale increases in the amount of electrons of solar origin [26].

The used quiet time electron spectrum was

$$I = \left(\frac{E}{E_1}\right)^{\gamma}, \tag{3.5.3.1}$$

where $\gamma = -3.61$ for energies between 0.2 MeV and 0.5 MeV, and $\gamma = -1.14$ for energies between 0.5 MeV and 1.996 MeV. For both cases $E_1 = 0.5$ MeV [26].

As for the cosmic ray protons, an intensity histogram was created to input the desired energy distribution to Geant4. Energies in the histogram were between 0.2 MeV and 1.996 MeV. The energy limits were calculated so that the energy range contains approximately 90 % of the total particle flux.

3.5.4 Results

The simulation outputs for protons and electrons were analysed in the same way as in section 3.4 with the same event categories and energy channels. Response to cosmic ray protons as a function of particle energy in proton energy channels is presented in Figure 3.14 (event categories C1–C5). Response to quiet time electrons as a function of particle energy in electron energy channels is presented in Figure 3.15 (event categories C1–C5).

The proton response shows non-ideal response to protons with energies higher than approximately 40 MeV, as seen in the flat spectrum acceptance results. Proton channels P5–P8 detect a high amount of high energy protons with energies between 60 MeV and 1 GeV. This non-ideal response is likely due to protons penetrating through the collimator structure and hitting the detector.

The electron channels are clean for quiet time electrons, as expected from the flat spectrum acceptance simulations.

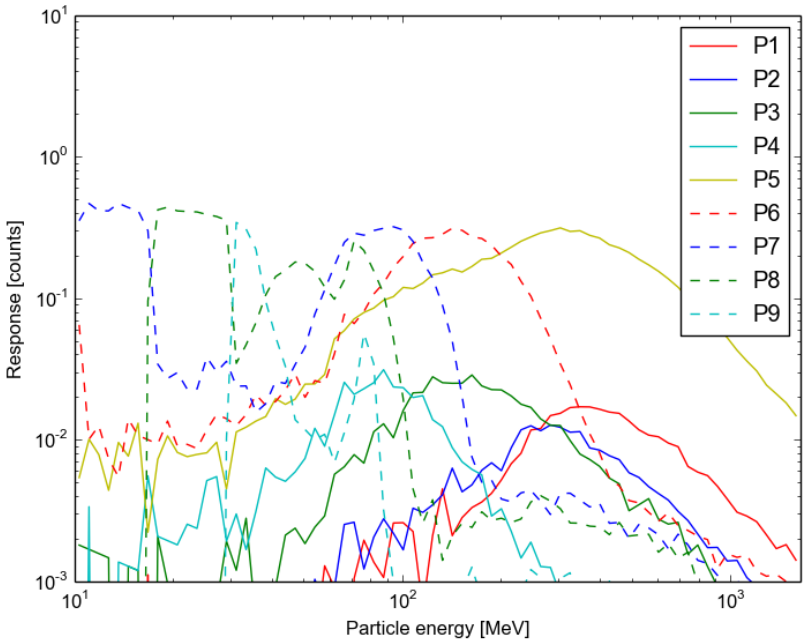

Figure 3.14: Response of the detector to cosmic ray protons in proton channels from event categories C1–C5.

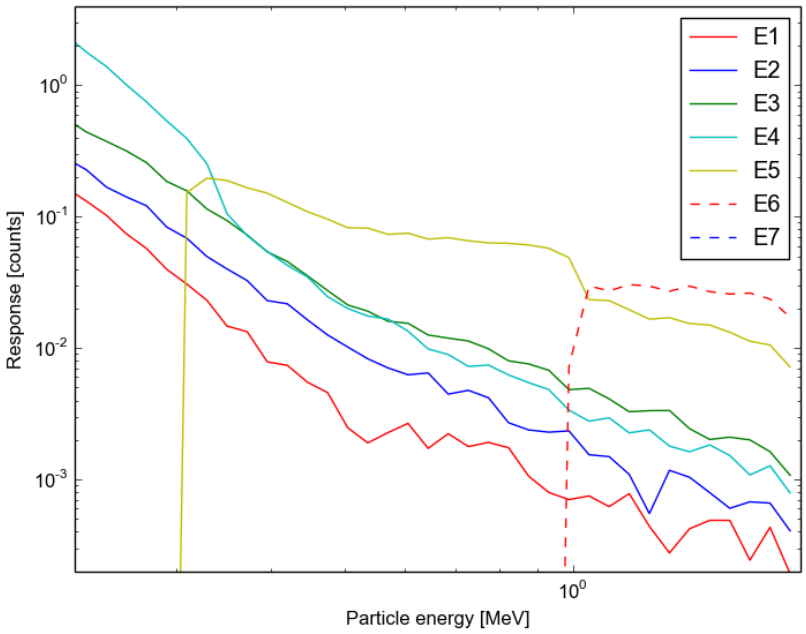

Figure 3.15: Response of the detector to an electron quiet time spectrum in electron channels from event categories C1–C5.

4 Lookup table

This chapter describes the method of producing a lookup table for the onboard data analysis of SIXS-P, the resulting lookup table, the particle response of the lookup table and the resulting energy channels. The use and theory of a lookup table is described in section 2.3.3. Spectral information extracted from a simulated solar electron event is presented in the last section of this chapter. The solar electron event simulation is based on an intense solar electron event measured by MESSENGER EPS.

4.1 Initial cell determination

The initial assignment of lookup table cells to energy channels was done with data from the acceptance simulations presented in section 3.4. Particle events in event categories C1–C5 were used to create the lookup table.

The energy channel's histogram counts (normalised to 1) were plotted as a function of particle energy. This was done separately for side only events, proton coincidence events and electron coincidence events. New energy channel limits for side only events and proton coincidence events were determined from these plots by finding the particle energy where the acceptance curves of adjacent energy channels cross. These limit energies for side only events are presented in Figure 4.1. The lower energy limits of P1 and P5 were determined individually to the particle energies where the response curve drops to half of the maximum value. The energy limits described in section 2.3.3 were used for the electron coincidence channels and 50 keV as the lower energy limit of channel E1. The energy channels used for the initial cell determination were:

- Electrons, single detector event. No hit in the core detector:
  - E1: 50–73 keV
  - E2: 73–110 keV

  - E3: 110–187 keV
  - E4: 187–1035 keV

- Electrons, coincidence event. Hit in the core detector:
  - E5: 300–1000 keV
  - E6: 1000–3000 keV
  - E7: $>$ 3000 keV

- Protons, single detector event. No hit in the core detector:
  - P1: 1.035–1.137 MeV
  - P2: 1.137–1.267 MeV
  - P3: 1.267–1.896 MeV
  - P4: 1.896–3.257 MeV

- Protons, single detector and coincidence events:
  - P5: 3.257–6.137 MeV

- Protons, coincidence event. Hit in the core detector:
  - P6: 6.137–10.14 MeV
  - P7: 10.14–17.276 MeV
  - P8: 17.276–30.178 MeV
  - P9: $>$ 30.178 MeV

1000 random particles from each energy channel were chosen to determine where the different energy channels are situated in the lookup table. The energy losses in the side and core detectors were transformed to 11-bit ADC values with the energy-ADC calibration parameters determined in section 3.3. As the electron core calibration could not be done due to the low number of experimental electron data, calibration parameters from an older calibration made by the author, with a different version of the SIXS-P, were used. The formula for converting electron core energy

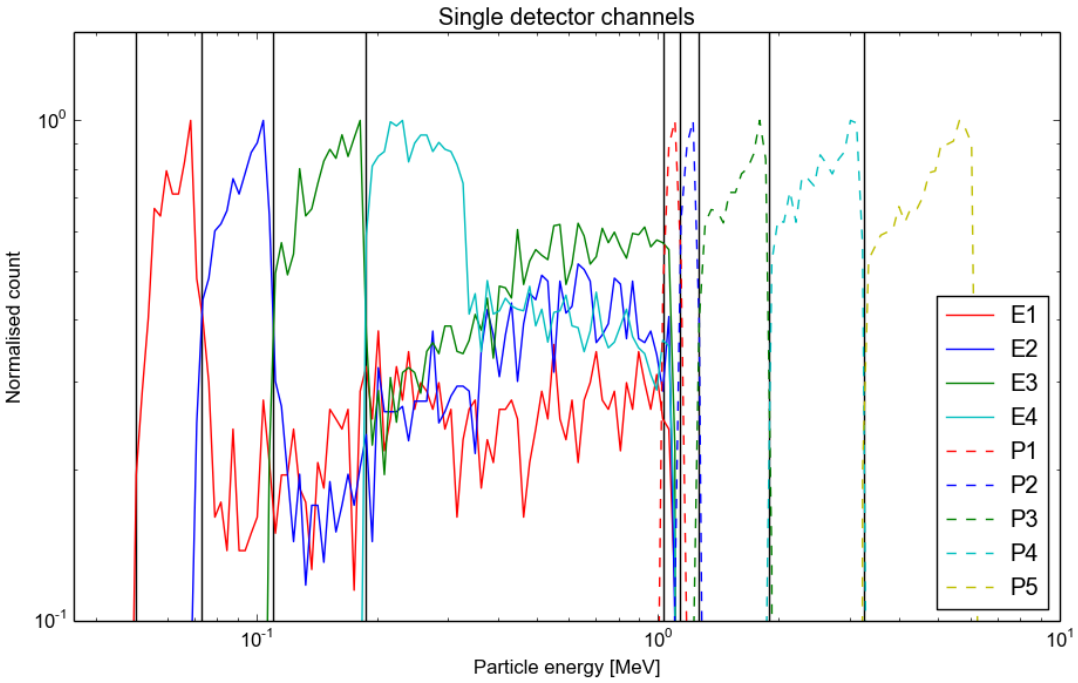

Figure 4.1: Normalised histogram counts of side only detector channels (E1–E4, P1–P5) as a function of particle energy. The histogram counts were normalised without dividing by bin widths to make the new channel limits easier to determine. The black vertical lines represent the new energy channel limits.

losses to 11-bit ADC values is:

$$ADC_{11-bit} = \text{ROUND}\Big(178.8581 + 15.5249 \cdot E^{2.5937}\Big), \tag{4.1.0.1}$$

where the energy loss in the core detector E is in MeV and the result is rounded to the closest integer. The same parameters were used for all electron coincidence events. The 11-bit ADC values were reduced to 8-bit ADC values with equation (2.3.3.1). The 8-bit values were bit shifted to the right by two to reduce the 8-bit values to 6-bit values.

The mode of energy channels in each cell of the lookup table was determined to find the right cells for each energy channel. The cells where the core detector 6-bit ADC is 0 were assigned to the side only channels. In the other cells, the selection was intentionally biased towards lower energy channels to avoid the higher energy channels dominating the lower energy channels at boundaries between different channels. The cell distribution of energy channels in the lookup table after the initial cell determination is presented in Figures 4.2 and 4.3.

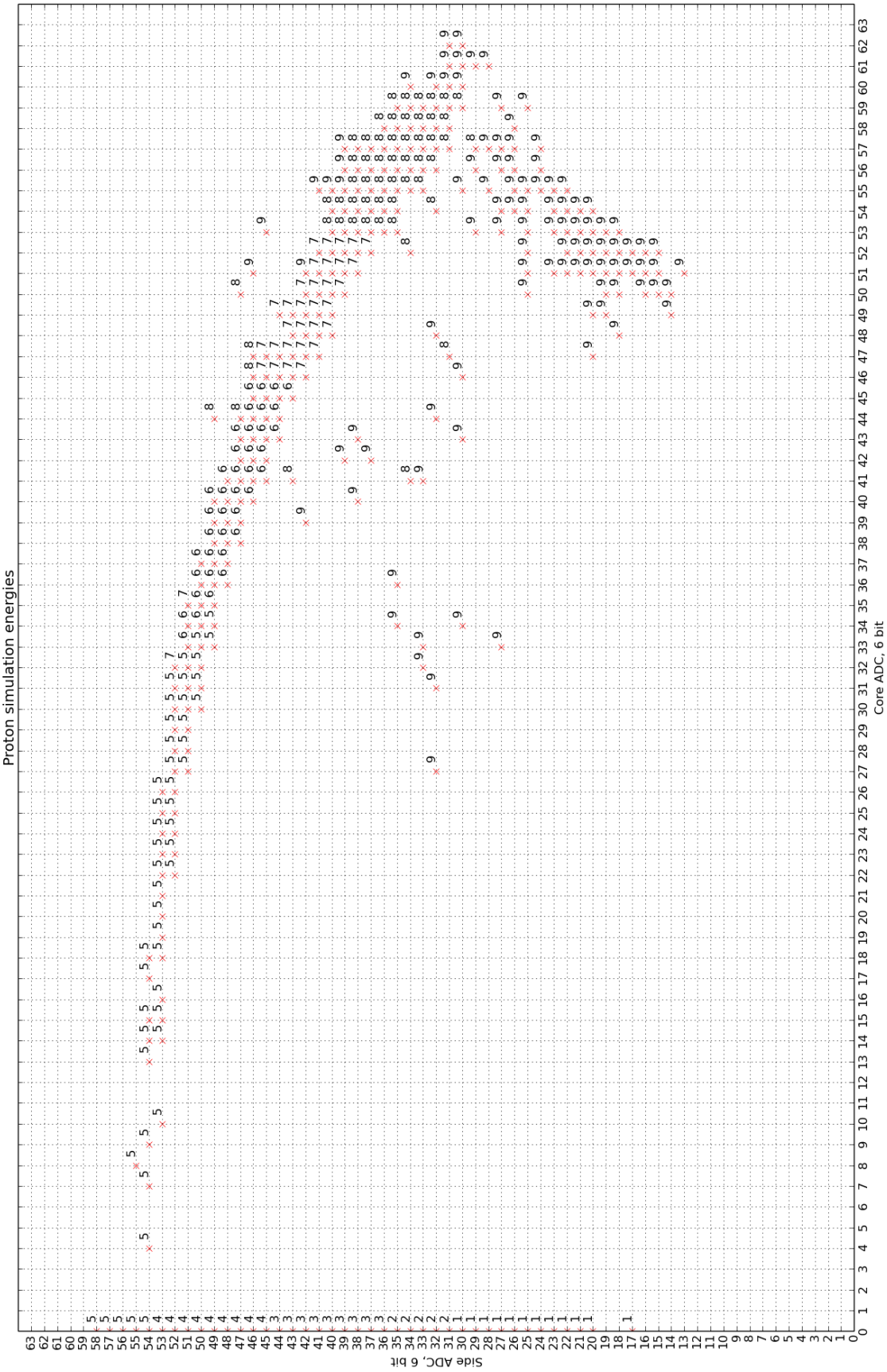

Figure 4.2: Distribution of proton channels in the lookup table after the initial cell determination.

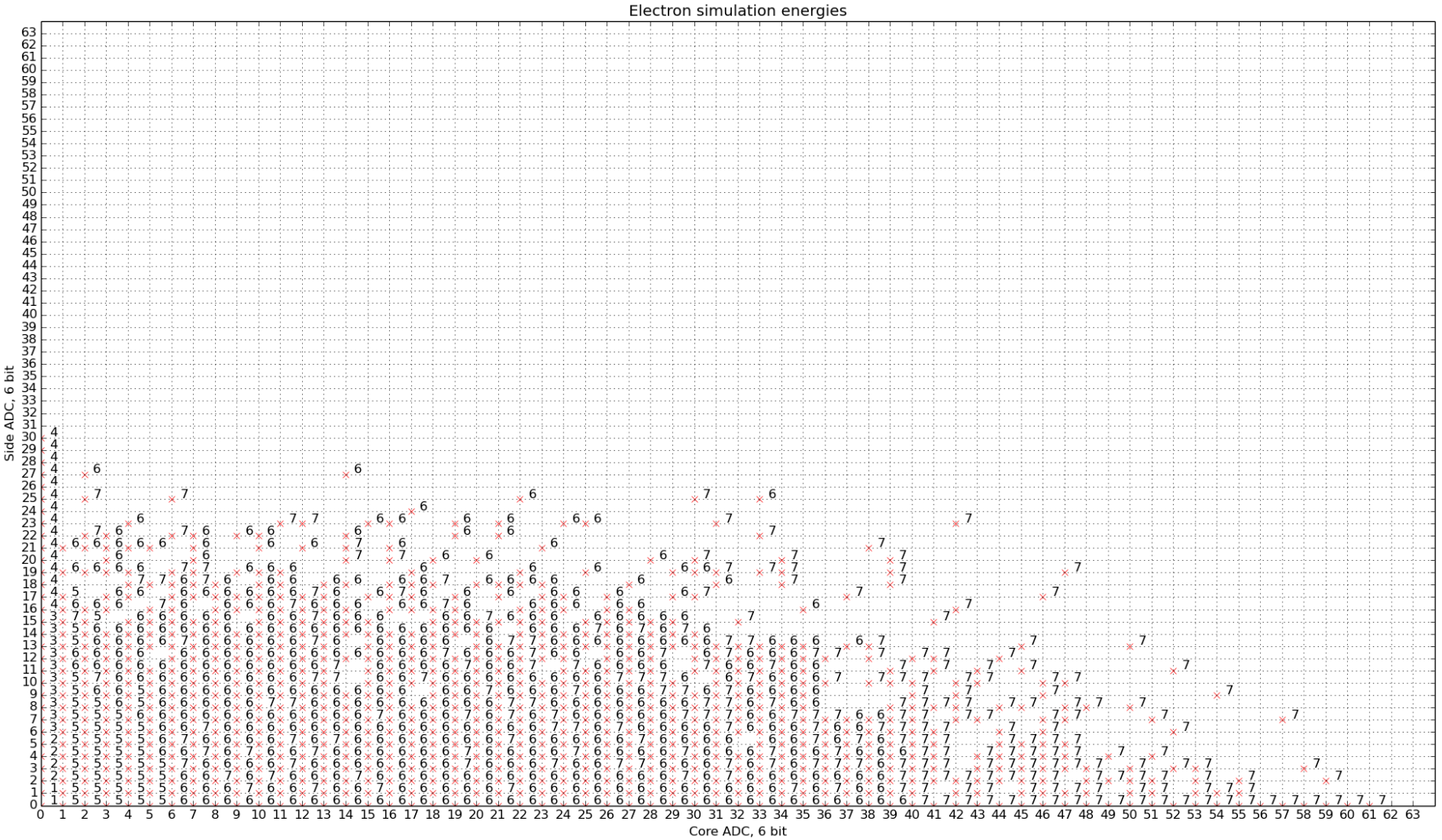

Figure 4.3: Distribution of electron channels in the lookup table after the initial cell determination.

The energy channel distribution was approximated from the initial cell determination. The energy channels were broadened and smoothened while maintaining the vertical boundaries between the different energy channels. The channels were broadened in both axis directions to take into account the temperature dependent response of the core scintillator and the statistical nature of the particle events. The electron side only channels were given priority in the overlap between the electron and proton boundaries in order to produce as clean proton side only channels as possible.

4.2 Lookup table response and cell adjustment

The initial lookup table was used to study the lookup table response and adjust the cells in the lookup table. The acceptance simulation data and additional simulation data were used to study the lookup table response.

Particle events from acceptance simulation data were separated into energy channels using the 6-bit ADC values of the events and the lookup table. The normalised counts in the energy channels were plotted as a function of particle energy. The cells that were not assigned to any proton or electron channels were designated as belonging to a 0 channel. The 0 channel can be used to see if a significant portion of the particles is not inadvertently detected. Sample plots of the lookup table response to protons and electrons are presented in Figures 4.4 and 4.5, respectively.

The positions of the energy channels in the lookup table were modified based on the response plots. The goal of this iteration process was to generate a lookup table that produces a flat energy channel response, detects most of the particles, and produces energy channels that are as close to the energy channels presented in section 2.3.3, as possible.

Additional high energy protons and electrons were simulated with the same setup as in the flat spectrum acceptance simulations. The energy ranges in the simulations were 100 MeV–400 MeV and 400 MeV–1000 MeV for protons and 6 MeV–100 MeV for electrons.

Electron events in proton channels were plotted in the same graph as proton events in proton channels to determine how much electrons contaminate the proton

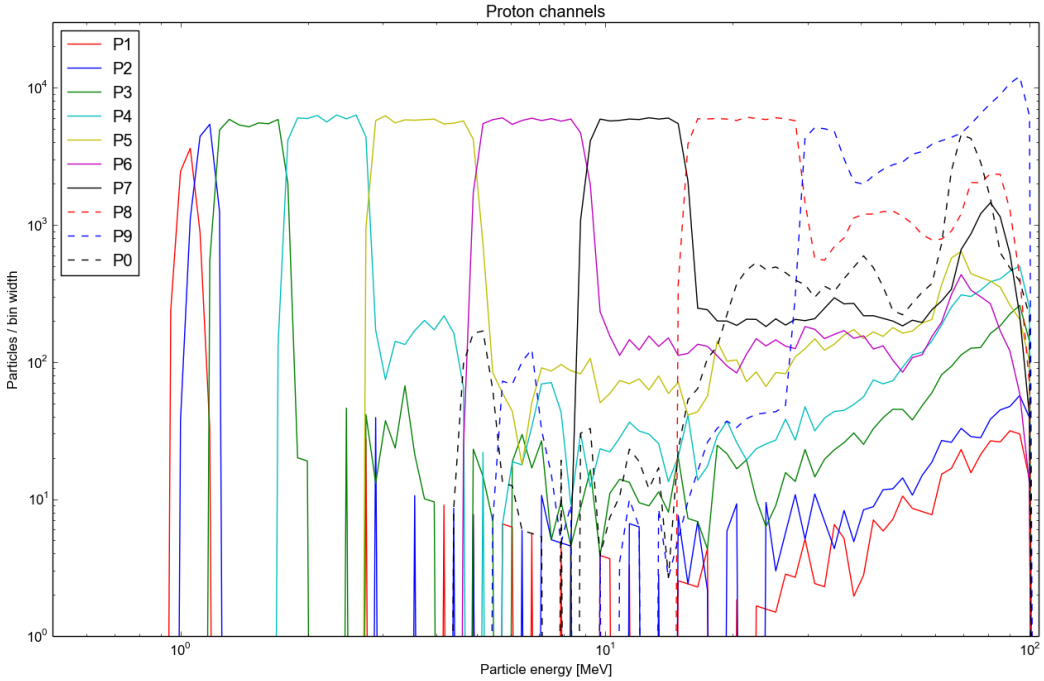

Figure 4.4: A sample lookup table response for different proton energy channels as a function of particle energy. Channel 0 is the response of the lookup table cells that are not assigned to any of the energy channels.

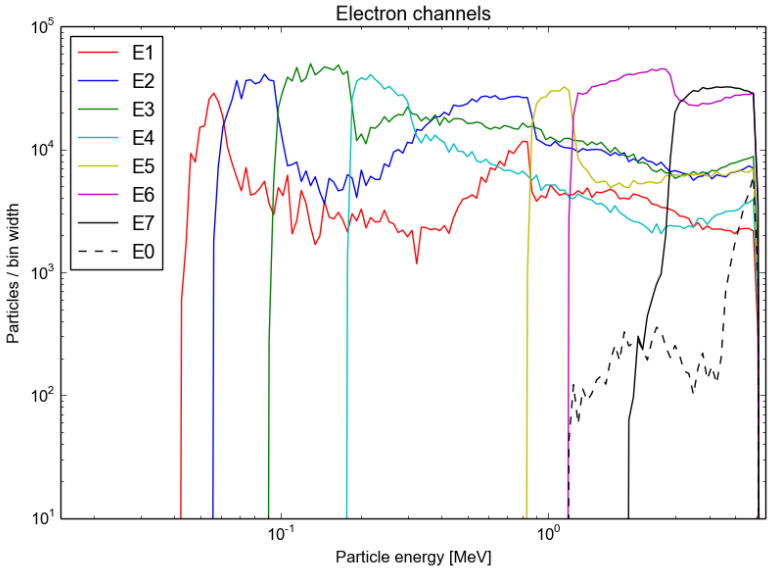

Figure 4.5: A sample lookup table response for different electron energy channels as a function of particle energy. Channel 0 is the response of the lookup table cells that are not assigned to any of the energy channels.

channels. The same process was repeated for protons in electron channels. The histograms were normalised with the normalisation factor G (see section 3.4.3), so that the electron and proton histograms are comparable.

Normalised proton and electron counts as a function of particle energy in proton channels are presented in Figure 4.6. Normalised electron and proton counts in electron channels are presented in Figure 4.7. These plots were also used to modify the position of the energy channels in the lookup table, where proton and electron channels are next to each other and overlap. Side only cells with electrons and protons were assigned to the electron channels as much as possible to produce clean proton side only channels.

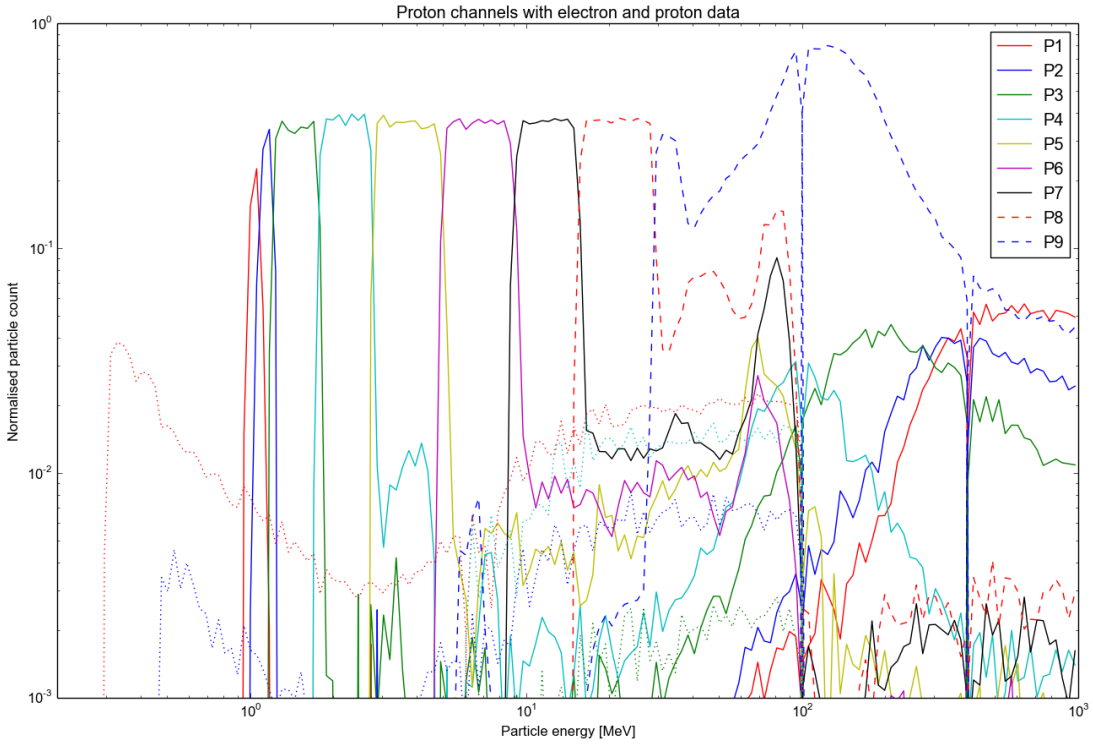

Figure 4.6: Proton and electron data divided into proton energy channels with the lookup table, and plotted as the normalised particle count as a function of particle energy. The dotted lines are the electron contributions to the proton channels. The discontinuities in the histograms are due to separate simulation runs.

The overlap of proton and electron side only events in the adjacent proton and electron channels is visible as an electron feature in P1 Figure 4.6 at approximately 300 keV.

The overlap of high energy electrons in channels E6 and E7 is clearly visible in Figure 4.7 above 6 MeV. A high number of high energy protons ($E > 100$ MeV)

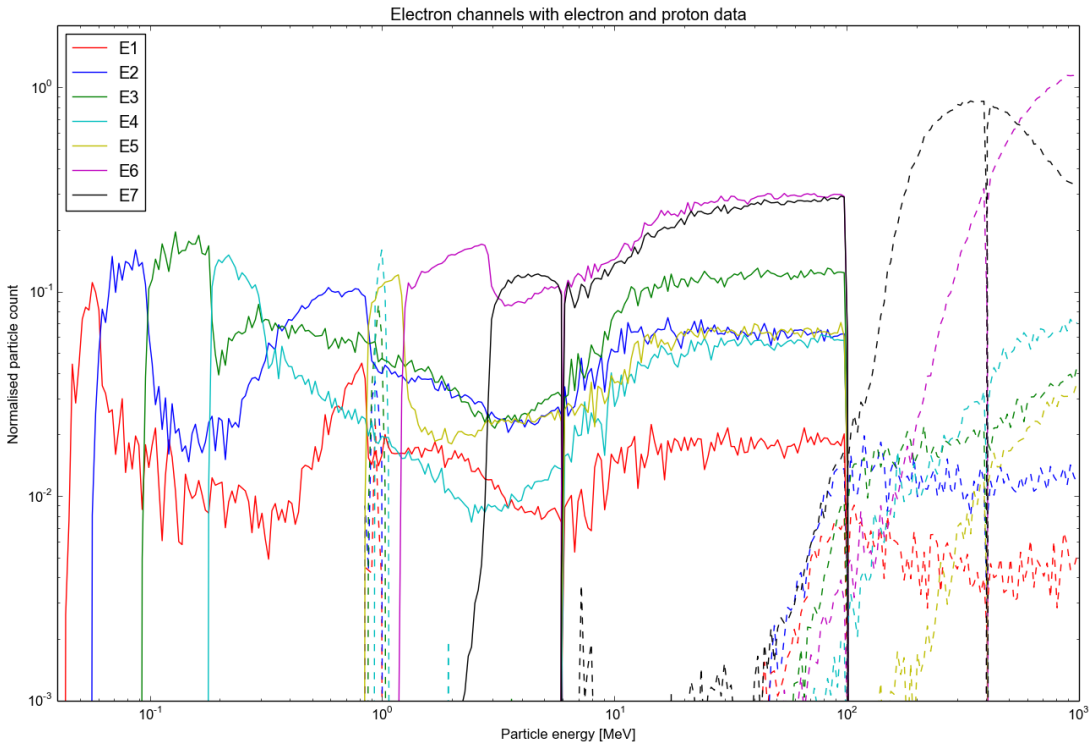

Figure 4.7: Electron and proton data divided into electron energy channels with the lookup table, and plotted as the normalised particle count as a function of particle energy. The dashed lines are the contributions of protons to the electron channels. The discontinuities in the histograms are due to separate simulation runs. A close-up of the proton contribution around 1 MeV is shown in Figure 4.8.

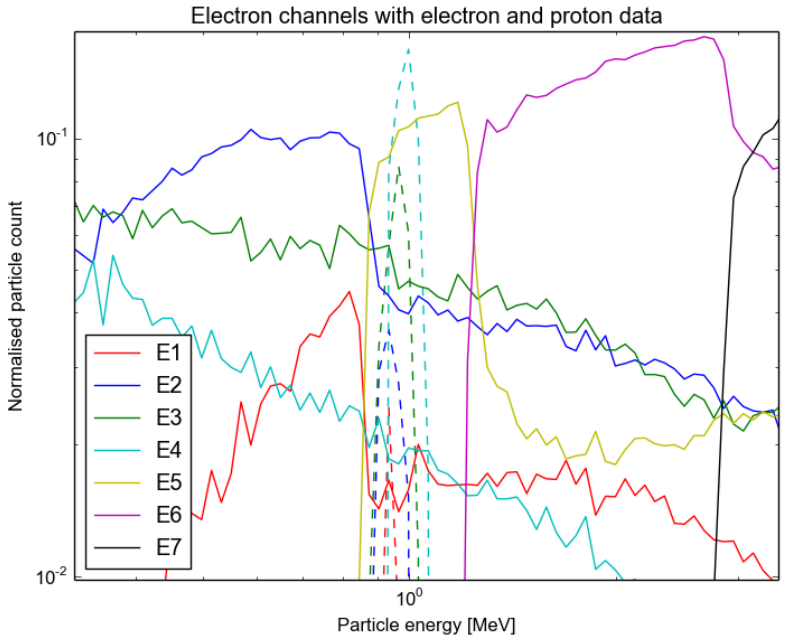

Figure 4.8: A close-up of Figure 4.7 showing the proton contamination of electron side only channels around 1 MeV. The solid lines are the electron contributions to electron channels and the dashed lines are the proton contributions. The electron channel proton spikes from top down are: E4, E3, E2, and E1.

are registered in electron channels E6 and E7, which is clearly visible due to the flat energy spectrum used in the simulations. The mixing of electron and proton side only events in the adjacent proton and electron channels is visible as a large spike of protons with energies approximately 0.9 MeV to 1.0 MeV in channel E4. Figure 4.8 shows a close-up of Figure 4.7 around this energy range. As the side only cells with mixed particle populations were assigned to electron channels, the contamination by protons in E4 is more prominent than the contamination by electrons in channel P1.

The discontinuities in the histograms at 6 MeV, 100 MeV and 400 MeV are caused by the separate simulation runs.

The final lookup table was produced with the described iteration process. The produced lookup table is presented in Figure 4.9. The resulting energy channels from this lookup table are:

- Electrons, single detector event. No hit in the core detector:
  - E1: 50–61 keV
  - E2: 61–98 keV
  - E3: 98–185 keV
  - E4: 185–305 keV
- Electrons, coincidence event. Hit in the core detector:
  - E5: 850–1240 keV
  - E6: 1240–3160 keV
  - E7: $>$ 3160 keV
- Protons, single detector event. No hit in the core detector:
  - P1: 0.99–1.07 MeV
  - P2: 1.07–1.21 MeV
  - P3: 1.21–1.77 MeV
  - P4: 1.77–2.77 MeV
- Protons, single detector and coincidence events:

  - P5: 2.77–4.96 MeV

- Protons, coincidence event. Hit in the core detector:
  - P6: 4.96–9.10 MeV
  - P7: 9.10–15.50 MeV
  - P8: 15.50–29.20 MeV
  - P9: $>$ 29.20 MeV

The lower limits of P1 and E5, and the upper limit of E4 were chosen as the points, where the particle count falls to half of the maximum value. The lower limit of E1 was chosen as 50 keV. The other energy limits were taken as the points where the energy channel response curve cross each other.

Compared with the nominal energy channels, the proton side only channels (P1–P4) are narrower, as the cells contaminated by electrons were assigned to the side only electron channels. The other energy channels follow the original energy channels as expected.

The flux channels for the instrument are chosen from the cleanest proton and electron channels. Based on the particle response of the instrument, the following flux channels can be used:

- Proton flux channels
  - FP1: P4 and P5
  - FP2: P6, P7 and P8
- Electron flux channel
  - FE: E3 and E5

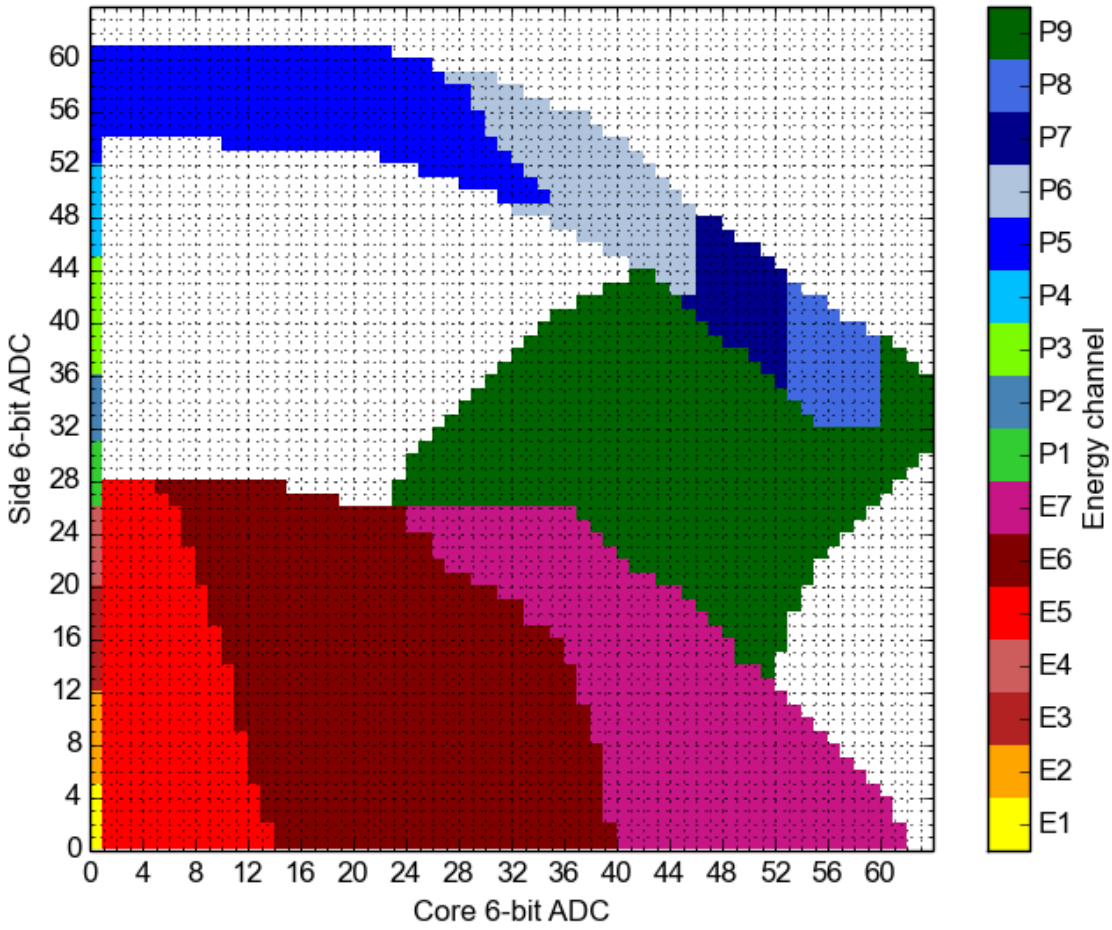

Figure 4.9: The produced lookup table for the instrument. The core detector 6-bit ADC value is on the vertical axis and the side detector 6-bit ADC value is on the vertical axis. The energy channel of a cell is indicated by the cell color. White indicates a spectral error cell.

4.3 MESSENGER events

An intense solar electron event from the 4$^{\text{th}}$ of June 2011 was simulated and analysed with a standard method to determine how well spectral information can be obtained with the lookup table. The data from the event was measured by the EPS instrument of the MESSENGER probe [27].

The event's approximate energy spectrum at flux maximum was determined by hand from MESSENGER EPS observations. The flux in an EPS energy channel was assumed to be the same as the flux at the geometric average of the channel boundaries. The fluxes were determined for each of the EPS energy channels and a fitting function

$$f(E) = cE^{-a}\mathrm{e}^{-b/E^d} \tag{4.3.0.2}$$

was fitted to the approximate spectrum to get the differential spectrum $\frac{dJ}{dE}$. The resulting energy spectrum of the event is presented in Figure 4.10. The resulting

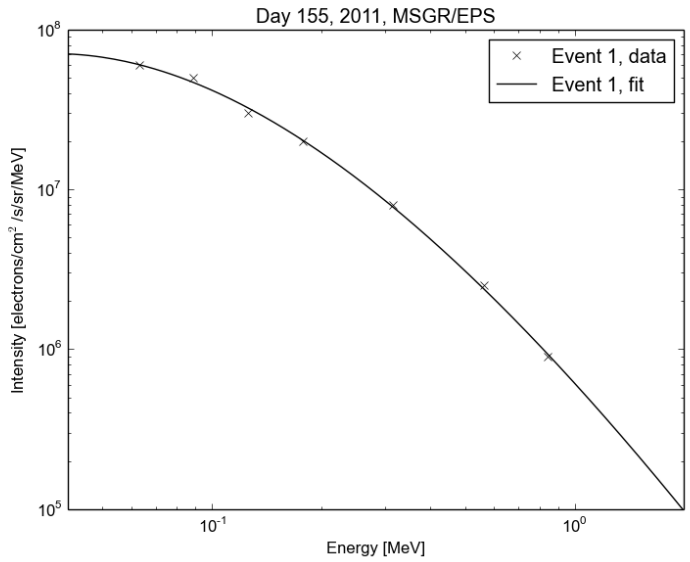

Figure 4.10: Energy spectrum of an intense solar energetic electron event measured by MESSENGER EPS on the 4$^{\text{th}}$ of June 2011.

fitting parameters for the function (4.3.0.2) are:

$$a = 4.1456, \quad b = 5.8819,$$
$$c = 2.1914 \cdot 10^8, \quad d = 0.27990$$

The event was simulated using Geant4 with a similar set-up as in section 3.4. Instead of a flat spectrum, an energy spectrum corresponding to the event's determined differential spectrum was used. The spectrum was created by giving Geant4 an input intensity histogram created with the function (4.3.0.2) and the determined fitting parameters from the event data. 160 000 000 electrons were simulated with this spectrum in the energy range 40 keV–10 MeV.

Electron data from the acceptance simulations presented in section 3.4 was divided into energy channels with the lookup table and normalised to units $\mathrm{cm}^2 \cdot$ sr by multiplying the particle counts in histogram bins with the normalisation factor G. The resulting acceptances $A_j(E)$ of electron channels E1 to E6 are shown in Figure 4.11. Subscript $j = 1, 6$ denotes the electron channel in question. Electron channel E7 was omitted, as it is an integral channel.

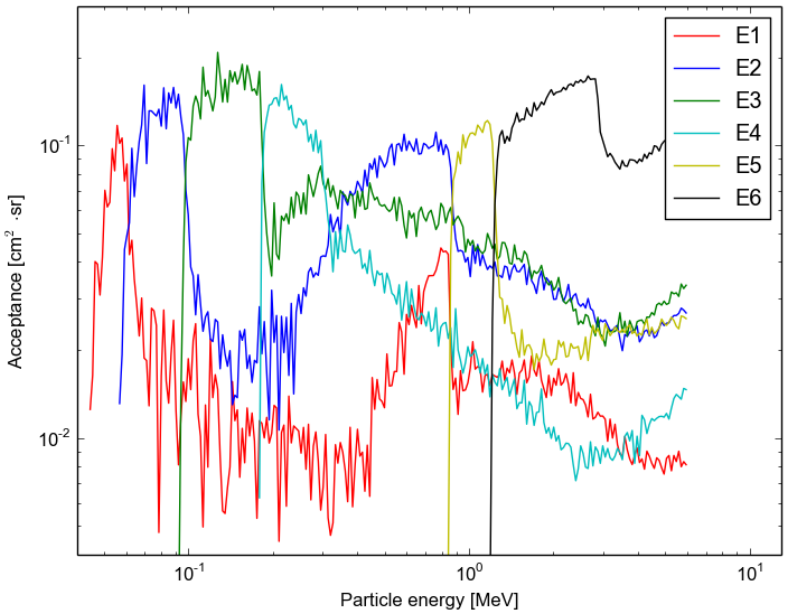

Figure 4.11: Electron acceptances A_j from the lookup table for electron channels E1 to E6.

Quantities $G_j \Delta E_j$ were calculated for each channel by integrating the accep-

tances $A_j(E)$ numerically from zero to the nominal upper limit of the energy channel:

$$G_j \Delta E_j = \int_0^{E_{2,j}} A_j(E)\, dE \tag{4.3.0.3}$$

The calculated quantities $G_j \Delta E_j$ for the electron channels E1–E6 are presented in Table 4.1. The simulated event data was divided into energy channels using the lookup table. Intensities in units electrons/cm^2/s/sr/MeV in each channel are:

$$I_j = \frac{N_j}{\Delta t \cdot G_j \Delta E_j}, \tag{4.3.0.4}$$

where N_j is the particle count in energy channel j as counted from the simulated event data with the lookup table and Δt has to be determined independently to normalise the intensities I_j to the input spectrum $\frac{dJ}{dE}$. The number of particles per time and energy unit is:

$$\frac{dN}{dE\, dt} = GF \cdot \frac{dJ}{dE}, \tag{4.3.0.5}$$

where GF is the geometric factor of the source (see section 3.4.3). The total number of simulated particles is:

$$N = \int_0^{\Delta t} \int_{E_0}^{E_\infty} \frac{dN}{dE\, dt}\, dE\, dt \tag{4.3.0.6}$$

$$= \Delta t \cdot GF \cdot \int_{E_0}^{E_\infty} \frac{dJ}{dE}\, dE. \tag{4.3.0.7}$$

Rearranging this we get the Δt:

$$\Delta t = \frac{N}{GF \cdot \int_{E_0}^{E_\infty} \frac{dJ}{dE}\, dE} \tag{4.3.0.8}$$

which can be inserted into equation (4.3.0.4) to get the normalised intensities:

$$\left(\frac{dJ}{dE}\right)_j = \frac{N_j \cdot GF \cdot \int_{E_0}^{E_\infty} \frac{dJ}{dE}\, dE}{N \cdot G_j \Delta E_j}. \tag{4.3.0.9}$$

The normalised intensity of each channel was plotted as a function of the geometric

midpoint of that energy channel $\langle E_j \rangle = \sqrt{E_{1,j} E_{2,j}}$ and function (4.3.0.2) was fitted to the plotted points. The points $\left(\langle E_j \rangle, (\frac{dJ}{dE})_j\right)$, the fitted function, and the event input spectrum are shown in Figure 4.12.

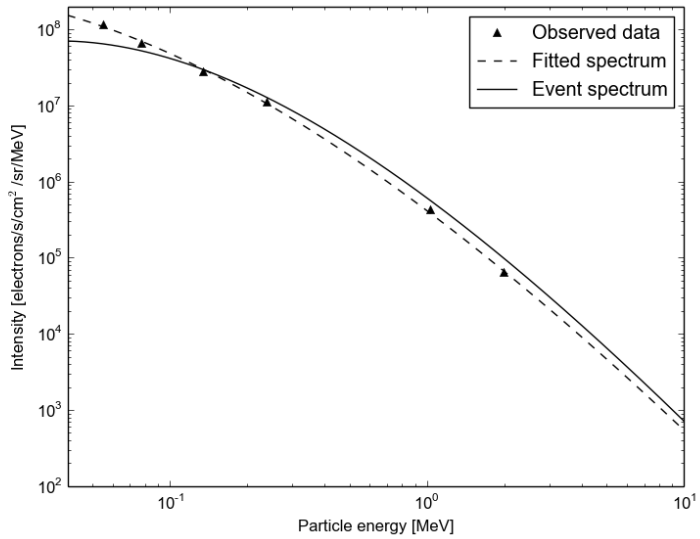

Figure 4.12: Comparison of the detected simulation electron spectrum (dashed line), and the input electron spectrum based on MESSENGER EPS observations (solid line). The intensity-geometric midpoint pairs are plotted as the triangles for each electron channel, as determined with the lookup table. Function (4.3.0.2) was fitted to the intensity-geometric midpoint pairs to produce the detected spectrum.

As seen from Figure 4.12, the detected electron spectrum follows the input spectrum rather poorly. The fitting parameters for the detected spectrum are:

$$a_{\text{det}} = 4.3816, \quad b_{\text{det}} = 9.7345,$$
$$c_{\text{det}} = 7.0240 \cdot 10^9, \quad d_{\text{det}} = 0.18972$$

The maximum absolute deviation of the detected spectrum from the input spectrum in the shown energy range is $8.3 \cdot 10^7$ electrons/cm^2/s/sr/MeV.

In an ideal case, the input spectrum and the observed spectrum are identical. Keeping the observed numbers of electrons in each channel fixed, the ideal case $G_j \Delta E_{j,\text{ideal}}$ can be calculated with the input spectrum. The input spectrum values at the geometric midpoints of the electron channels are:

$$\left(\frac{dJ}{dE}\right)_{j,\text{input}} = \frac{dJ}{dE}(\langle E_j \rangle) \tag{4.3.0.10}$$

By rearranging equation (4.3.0.9) for $G_j \Delta E_j$ and using $\left(\frac{dJ}{dE}\right)_{j,\text{input}}$ instead of the observed normalised intensities, the ideal $G_j \Delta E_j$ can be calculated as:

$$G_j \Delta E_{j,\text{ideal}} = \frac{N_j \cdot GF \cdot \int_{E_0}^{E_\infty} \frac{dJ}{dE}\, dE}{N \left(\frac{dJ}{dE}\right)_{j,\text{input}}} \tag{4.3.0.11}$$

Quantities $G_j \Delta E$ of the instrument channels and the ideal case $G_j \Delta E_{j,\text{ideal}}$ are presented in Table 4.1.

Table 4.1: Calculated quantities $G_j \Delta E_j$ for the instrument electron channels and $G_j \Delta E_j$ for an ideal case where the detected spectrum is identical to the input spectrum.

Channel	$G_j \Delta E_j$ [cm^2· sr · MeV]	$G_j \Delta E_{j,\text{ideal}}$ [cm^2· sr · MeV]
E1	0.000984	0.00179
E2	0.00442	0.00562
E3	0.0134	0.0125
E4	0.0140	0.0123
E5	0.0368	0.0275
E6	0.264	0.170

The input spectrum cannot be determined from the observed electron channel counts with the used standard analysis method. The instrument channels are too integral for the standard method. A different method should be developed, tested, and used to extract spectral information from the energy channel particle counts.

5 Conclusions and acknowledgements

5.1 Conclusions

The energy response of the SIXS-P detector for electrons and protons was calibrated using experimental data and Geant4 simulations. The side detector energy response to electrons and protons was found to be linear, and the core scintillator energy response to protons non-linear. The energy response calibration of the core scintillator for electrons was omitted due to insufficient experimental data.

The acceptance of the SIXS-P detector for protons and electrons was simulated with the Geant4 software. Proton channels are clean in the nominal energy range, but protons with energies higher than approximately 40 MeV produce non-ideal response in all channels apart from channel P9. Electron channels are clean in the nominal energy range apart from channels E6 and E7. Channel E6 measures approximately as much electrons with energies belonging to channel E7 as channel E7. This overlap in channels E6 and E7 is likely due to backscattering electrons and energy loss from the detector due to Bremsstrahlung. The acceptances of both, electrons and protons, exhibit a lot of statistical variation, which is caused by the relatively low number of detected particles for the used simulation set-up. More stable acceptances could be achieved by simulating monoenergetic particles. Energies for these simulations should be selected using the present work as guideline to achieve good energy coverage where the acceptance curves are changing rapidly as a function of energy. The monoenergetic approach should be used in future work to produce smoother acceptance curves for electrons and protons.

The acceptances of the SIXS-P detector for cosmic ray protons and quiet time Jovian electrons were simulated by using intensity fluxes from literature. As expected from the flat spectrum results, protons with higher energies than 40 MeV produce non-ideal response. Protons with energies between 60 MeV and 1000 MeV produce a large amount of non-ideal response in proton channels P5 to P8. The electron channels are clean, as expected from the flat spectrum acceptance results.

A lookup table was produced for the onboard data analysis of the instrument, and the particle response of the lookup table was analysed. The 64×64 cell lookup table divides detected particles into energy channels based on the detected 6-bit ADC pulse heights from the side and core detectors. The cells in the lookup table were adjusted so that the lookup table identifies most of the particles, and produces energy channels that are clean and close to pre-defined energy channels. Based on the particle response of the lookup table, the SIXS-P instrument will be able to identify most electrons and protons in the required energy ranges. SIXS-P is required to monitor counting rates of electrons and protons with high time resolution in a couple of energy bands. Suitable proton channel combinations for these proton flux channels are: P4 and P5, and P6, P7 and P8. Suitable electron channel combination for an electron flux channel is E3 and E5.

The ability of the lookup table to extract spectral information of the incident flux was studied by analysing a simulated solar electron event with a standard analysis method. The input electron spectrum could not be inferred from the electron channel particle counts with the used method, as the electron channels of the instrument are too integral. A different method should be studied and used in the future for the extraction of spectral information from the channel particle counts. This different method could make use of counts in all nominal energy channels simultaneously to deduce the intensities in these channels.

5.2 Acknowledgements

I would like to thank Prof. Rami Vainio and Jussi Lehti for their help, advice, and supervision during the writing of this thesis and during my employment in the Space Research Laboratory (SRL) of the University of Turku and in Aboa Space Research (ASRO). I would like to express my gratitude to the employees of SRL and ASRO for their advice during my studies and employment.

The Geant4 simulations and parts of the data analysis presented in this thesis were made while employed by ASRO. The lookup table was produced while employed by SRL.

The experimental SIXS-P data used in this thesis were measured and provided

by ASRO. Experimental MESSENGER EPS data was provided by Dr. David Lario of the Applied Physics Laboratory of the Johns Hopkins University. The original Geant4 model of the SIXS-P detector was written by Jussi Lehti.

Bibliography

[1]J. Benkhoff, J. van Casteren, H. Hayakawa, et al., "BepiColombo—Comprehensive exploration of Mercury: Mission overview and science goals", Planetary and Space Science **58**, 2 –20 (2010).

[2]A. Balogh, R. Grard, S. Solomon, et al., "Missions to Mercury", Space Science Reviews **132**, 611–645 (2007).

[3]D. L. Shirley, "The Mariner 10 mission to Venus and Mercury", Acta Astronautica **53**, 375 –385 (2003).

[4]D. Moessner and J. McAdams, "Design, implementation, and outcome of MESSENGER's trajectory from launch to Mercury impact", Astrodynamics Specialist Conference, American Astronautical Society **15-608** (2015).

[5]R. L. McNutt, S. C. Solomon, P. D. Bedini, et al., "MESSENGER at Mercury: Early orbital operations", Acta Astronautica **93**, 509 –515 (2014).

[6]R. Grard and A. Balogh, "Returns to Mercury: Science and mission objectives", Planetary and Space Science **49**, 1395 –1407 (2001).

[7]A. Anselmi and G. E. Scoon, "BepiColombo, ESA's Mercury Cornerstone mission", Planetary and Space Science **49**, 1409 –1420 (2001).

[8]European Space Agency (ESA), *Mission Operations - Getting to Mercury*, `http://sci.esa.int/bepicolombo/48871-getting-to-mercury/`, 2016, accessed: June 2016.

[9]J. Huovelin, R. Vainio, H. Andersson, et al., "Solar Intensity X-ray and particle Spectrometer (SIXS)", Planetary and Space Science **58**, 96 –107 (2010).

[10]A. Milillo, M. Fujimoto, E. Kallio, et al., "The BepiColombo mission: An outstanding tool for investigating the Hermean environment", Planetary and Space Science **58**, 40 –60 (2010).

[11]G. Fraser, J. Carpenter, D. Rothery, et al., "The Mercury Imaging X-ray Spectrometer (MIXS) on BepiColombo", Planetary and Space Science **58**, 79 –95 (2010).

[12]S. N. Ahmed, *Physics and engineering of radiation detection*, Second edition (Elsevier, 2015).

[13]R. A. Mewaldt, C. M. S. Cohen, W. R. Cook, et al., "The Low-Energy Telescope (LET) and SEP central electronics for the STEREO mission", Space Science Reviews **136**, 285–362 (2008).

[14]E. Stone, C. Cohen, W. Cook, et al., "The Solar Isotope Spectrometer for the Advanced Composition Explorer", Space Science Reviews **86**, 357–408 (1998).

[15]J. Huovelin and ESA/ASD P/L Team, *SIXS experiment interface document, BC-EST-RS-02518* (2014).

[16]S. Korpela, *BepiColombo SIXS engineering plan, BC-SIX-PL-00003* (2011).

[17]J. Huovelin, W. Schmidt, M. Genzer, et al., "SIXS: X-ray and particle instrument on BepiColombo", European Planetary Science Congress 2013 **8**, EPSC2013–112 (2013).

[18]J. Lehti, Private communication, 2016.

[19]J. Lehti and J. Saari, *SIXS FS proton measurement calibration, BC-SIX-TR-02050* (2014).

[20]R. Vainio and E. Esko, *On-board data handling system of BC/SIXS, BC-SIX-TN-00014* (2009).

[21]S. Agostinelli, J. Allison, K. Amako, et al., "Geant4 — A simulation toolkit", Nuclear Instruments and Methods in Physics Research Section A: Accelerators, Spectrometers, Detectors and Associated Equipment **506**, 250 –303 (2003).

[22]J. Lehti, *Simulations of SIXS-P EM model, BC-SIX-TN-02025* (2009).

[23]J. Lehti and J. Saari, *SIXS FS electron measurement calibration, BC-SIX-TR-02049* (2014).

[24]Z. Yun-Long, W. Xiao-Lian, and X. Zi-Zong, "Evaluation of particle acceptance for space particle telescope", Chinese Physics C **35**, 774 (2011).

[25]R. Vainio, L. Desorgher, D. Heynderickx, et al., "Dynamics of the Earth's particle radiation environment", Space Science Reviews **147**, 187 –231 (2009).

[26]P. Kühl, N. Dresing, P. Dunzlaff, et al., "Spectrum of galactic and Jovian electrons", Proceedings of the 33rd International Cosmic Rays Conference **0072** (2013).

[27]D. Lario, Private communication, 2014.